A hydro-osmotic coarsening theory of biological cavity formation

Mathieu Le Verge–Serandour[1] **and Hervé Turlier**[1*]

***For correspondence:** herve.turlier@college-de-france.fr (FMS)

[1]Center for Interdisciplinary Research in Biology, Collège de France, PSL Research University, CNRS UMR7241, INSERM U1050, 75005 Paris, France.

Abstract Fluid-filled biological cavities are ubiquitous and the formation of apical lumens is widely studied. But the physical mechanism underlying basolateral cavity emergence, such as blastocoels or cysts, remains unclear. We propose a model where a single cavity results from the coarsening of a network of micrometric lumens interconnected through the intercellular space. Cavity formation is found to be primarily controlled by hydraulic exchanges, with a minor influence of osmotic heterogeneities. The coarsening dynamics is self-similar with a dynamic scaling exponent reminiscent of dewetting films over a large range of ion and water permeabilities. Adding active ion pumping to account for lumen growth enriches the dynamics: it prevents from collective collapse and leads to the emergence of a novel coalescence-dominated regime exhibiting a distinct scaling law. Finally, we prove that spatially biasing ion pumping may be sufficient to position the cavity, suggesting a novel mode of symmetry breaking for tissue patterning.

Introduction

Biological cavities, also known as lumens, are ubiquitous in tissues, organs and embryos. Common mechanisms for the formation of lumens at the apical side of polarized cells are described in various model systems ***Sigurbjörnsdóttir et al.*** (***2014***), but the emergence of basolateral cavities, also called cysts in tissues, or blastocoels in early embryos, has received much less attention. Apical lumens are facing intrinsically non-adherent cell interfaces ***Zhang et al.*** (***2020***) and are directly sealed at their surface by tight junction proteins ***Krug et al.*** (***2014***), limiting paracellular water leaking from the cavity into the intercellular space, while allowing for the passage of selected ions ***Narayanan et al.*** (***2020***). This may explain why tissues with multiple apical lumens may fail to spontaneously resolve into a single cavity ***Torkko et al.*** (***2008***). In contrast, the basolateral side of cells is most generally adhesive and blastocoel-like cavities need to grow against adhesive contacts. This important topological difference may explain why basolateral cavities systematically appear pressurized. Since there is no tight junctions, basolateral cavities further communicate directly with the intercellular space, where the pressurized fluid may flow and ions may diffuse. This manuscript aims therefore at describing from a theoretical perspective the physics of water and ion exchanges between cavities and the intercellular space to explain cavity morphogenesis.

In vitro, MDCK monolayers spontaneously generate fluid-filled domes at their basolateral surface (also called blisters) when they are plated on a 2D glass surface ***Cereijido et al.*** (***1978***); ***Lever*** (***1979***), and cysts in 3D when they are maintained in suspension ***Wang et al.*** (***1990***, 1994). This process is characterized by active ion pumping toward the basal side of cells, triggering water uptake in the apico-basal direction. In vivo, blastocoel emergence is classically described as the outcome of cell cleavage patterning, where successive divisions take place along the surface plane of the embryo to direct the organization of blastomeres in a spherical sheet ***Wolpert et al.*** (***2015***), such as in cnidarians or echinoderms ***Gustafson and Wolpert*** (***1961***); ***Dan-Sohkawa and Fujisawa*** (***1980***).

In this scenario, supported by numerical simulations ***Drasdo and Forgacs*** (***2000***); ***Bodenstein*** (***2020***), the first cleavages leave an initial intercellular space between loosely adhering blastomeres, that is amplified in volume by consecutive planary-oriented divisions, requiring the free movement of water through the nascent epithelial layer to fill the central cavity. But in various vertebrate embryos such as mammals (eutherians) ***Eckert and Fleming*** (***2008***), and, to a certain extent, amphibian embryos ***Merzdorf et al.*** (***1998***), the epithelial layer may be already sealed by tight junctions before blastocoel formation, making the emergence of a cavity by division patterning alone unclear. Recently, we uncovered an alternative mechanism in mouse embryos ***Dumortier et al.*** (***2019***), whereby adhesive contacts are hydraulically fractured into myriad of microcavities (also called microlumens) that progressively coarsen into a single cavity, most likely through fluid exchange within the $\sim 50\mathrm{nm}$ wide intercellular space ***Miyaguchi*** (***2000***); ***Fenz et al.*** (***2009***) (Fig. 1). In fact, similar micron-sized fluid-filled compartments had already been observed at the cell-cell contacts of various embryos preceding blastula formation: in mammals ***Fléchon et al.*** (***1976***); ***Hurst et al.*** (***1978***), in amphibians ***Tuft*** (***1965***); ***Kalt*** (***1971***); ***Barua et al.*** (***2017***) and even in *C.elegans*, although for the latter the resulting cavity rapidly disappears ***Nance and Priess*** (***2002***). Such transient coarsening phase may have been missed in other species having a tightly compacted morula prior to blastula stage, because of the need to image section planes of the embryo with a high spatiotemporal resolution. In this alternative mechanism, the fluid is pumped by an osmotic gradient from the external medium into the intercellular space, highlighting an evident coupling between hydraulic and osmotic effects. The requirement of ion pumping was, in fact, already well documented in mammalian embryos ***Borland et al.*** (***1977***); ***Wiley*** (***1984***); ***Mazur and Schneider*** (***1986***); ***Barcroft et al.*** (***2003***); ***Kawagishi et al.*** (***2004***), and some evidence of osmotic control of cavity formation in other embryo types was already put forward earlier ***Dan*** (***1952***); ***Løvtrup*** (***1960***); ***Beadle*** (***1969***). Yet, little is known about the hydro-osmotic control of cavity formation from a physics perspective.

Hydraulic and osmotic flows are indeed more and more recognized as essential determinants of embryo and tissue shaping ***Dasgupta et al.*** (***2018***); ***Lamiré et al.*** (***2020***); ***Chan et al.*** (***2019***); ***Dumortier et al.*** (***2019***); ***Narayanan et al.*** (***2020***); ***Alsous et al.*** (***2021***); ***Chartier et al.*** (***2020***). However only a few physical models describe the interplay between cell mechanics, osmotic effects and fluid flow in morphogenesis ***Alim*** (***2018***); ***Cheddadi et al.*** (***2019***); ***Dolega et al.*** (***2021***); ***Long et al.*** (***2020***) and in previous models, osmolarity is mostly considered spatially homogeneous. Here, we propose a generic hydro-osmotic physical model that explicitly accounts for ion pumping and osmotic gradients. We do not study, however, the nucleation process of the first cavities, which likely involves a hydraulic fracturation of cell-cell contacts ***Arroyo and Trepat*** (***2017***). We start on the contrary from a preformed and contiguous network of microlumens (Figs. 1A-B) and we focus on their collective dynamics using numerical simulations and mean-field theory. For the sake of simplicity, we also neglect ion charges and membrane potentials and consider a single solute only, following similar hypotheses as a recent model for a single apical lumen ***Dasgupta et al.*** (***2018***).

Results

Coupled dynamics for two lumens

In this first section, we focus on a two lumens system to introduce the fundamental dynamic equations and to characterize the competition between hydraulic and osmotic effects.

Dynamical equations

Dynamical equations for two lumens are derived from conservation equations of mass and solutes. The lumens are represented as 2-dimensional compartments connected through a 1-dimensional bridge of width e_0 and length ℓ along the x-direction (Fig. 1D). Each lumen $i = 1, 2$ is described by its area A_i, its hydrostatic pressure P_i and its concentration $C_i = \frac{N_i}{A_i}$, supposed homogeneous, where N_i is the number of solutes (in moles). A lumen is pressurized by a tension γ supposed constant, leading to a Laplace's pressure jump $\delta P_i = P_i - p_0 = \gamma \sin\theta / \sqrt{\mu A_i}$ across the membrane, where μ is a constant that depends on the contact angle $\theta = \arccos \gamma_c / 2\gamma$ between the lumens and

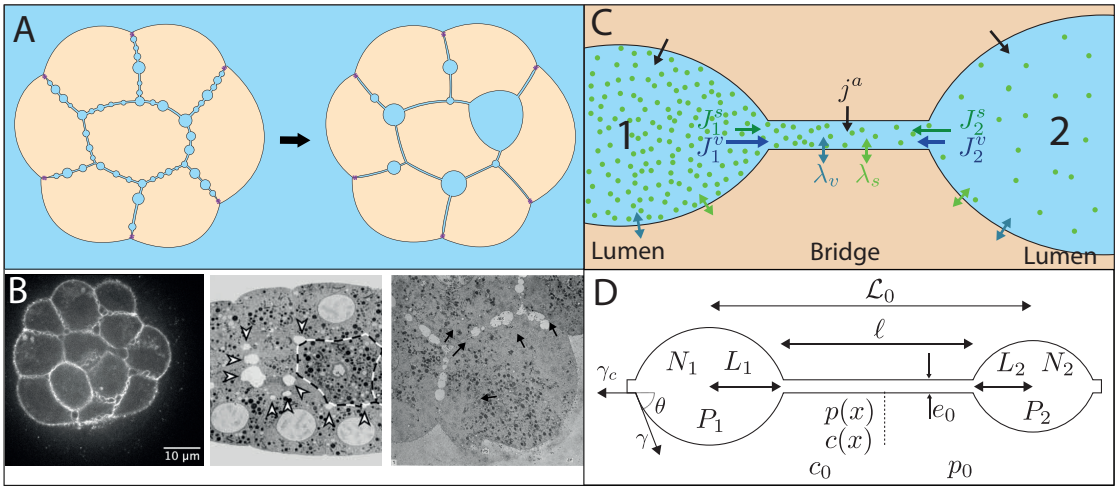

Figure 1. Network of microlumens in embryos and description of the model. (A) Schematic of the coarsening process to explain the formation of a single blastocoel cavity from a network of microlumens. (B) Examples of microlumen networks in various early embryos. Left: fluorescence microscopy confocal section of a mouse embryo at 32-cell stage ***Dumortier et al.*** (***2019***). Center: Electron micrograph of a 28-cell *C.elegans* embryo ***Nance and Priess*** (***2002***). Right: Electron micrograph of a 9-cell rhesus monkey embryo ***Hurst et al.*** (***1978***). (C) Lumens are modeled as distinct compartments interconnected through an intercellular bridge. They can exchange water (v) and solutes (s) with each others through the bridge (fluxes J_i^v and J_i^s) and with surrounding cells by active pumping of rate j^a and through passive permeation of coefficients λ_v, λ_s . (D) Parametrization of the two-lumen system: each lumen is characterized by its length $L_i = (\mu A_i)^{1/2}$, concentration C_i and pressure P_i; the intercellular bridge is characterized by its length $\ell(t)$, thickness e_0, and position-dependent solute concentration $c(x)$ and hydrostatic pressure $p(x)$.

the bridge with γ_c the adhesive tension in the bridge (see Appendix 1 and Fig. 1D). The lumens and the bridge are delimited by two lateral membranes of water and solutes permeability coefficients λ_v and λ_s respectively and are embedded in a an infinite "cellular" medium acting as a chemostat of concentration c_0 and as a barostat of pressure p_0 (Fig. 1C). The mass in a lumen i is modified through a longitudinal hydraulic flux J_i^v toward the bridge and through lateral osmotic fluxes from the cellular medium, that stem from the imbalance between osmotic and hydraulic pressure across membranes. We rewrite mass balance as function of the lumen length $L_i = \sqrt{\mu A_i}$

$$\frac{dL_i}{dt} = 2\mu\nu\lambda_v\left[\mathcal{R}T\delta C_i - \delta P_i\right] - \frac{\mu}{2L_i}J_i^v, \tag{1}$$

where $\mathcal{R}$ is the gas constant, T the temperature, $\delta C_i = C_i - c_0$ is the concentration jump across the membranes, and ν is a geometrical constant function of θ (see Appendix 1). The hydraulic flux J_i^v is calculated from boundary conditions in the bridge. The number of moles of solutes in each lumen N_i similarly varies through an outgoing flux J_i^s toward the bridge and through lateral passive fluxes, triggered by the chemical potential difference of the solute across membranes. Adding an active pumping rate j^a by unit membrane length, solute balance reads

$$\frac{dN_i}{dt} = 2\nu L_i\left[\lambda_s\mathcal{R}T\log\left(\frac{c_0}{C_j}\right) + j^a\right] - J_i^s \tag{2}$$

Conservation equations in the bridge are written along its length $\ell(t)$ in the x-direction. Local mass balance is obtained by calculating incoming and outgoing longitudinal fluxes along the x-axis and lateral osmotic fluxes across the membranes. The longitudinal flux is given by the 2D Poiseuille's flow $q(x) = -\kappa_v\frac{\partial\delta p}{\delta x}$, where $\kappa_v \approx \frac{e_0^3}{12\eta}$ is the hydraulic conductivity, inversely proportional to the solvent viscosity η. Considering a passive lateral flux of solvent along the two membrane sides, like for the lumens, yields

$$\kappa_v\frac{\partial^2\delta p}{\partial x^2} + 2\lambda_v\left[\mathcal{R}T\delta c(x) - \delta p(x)\right] = 0 \tag{3}$$

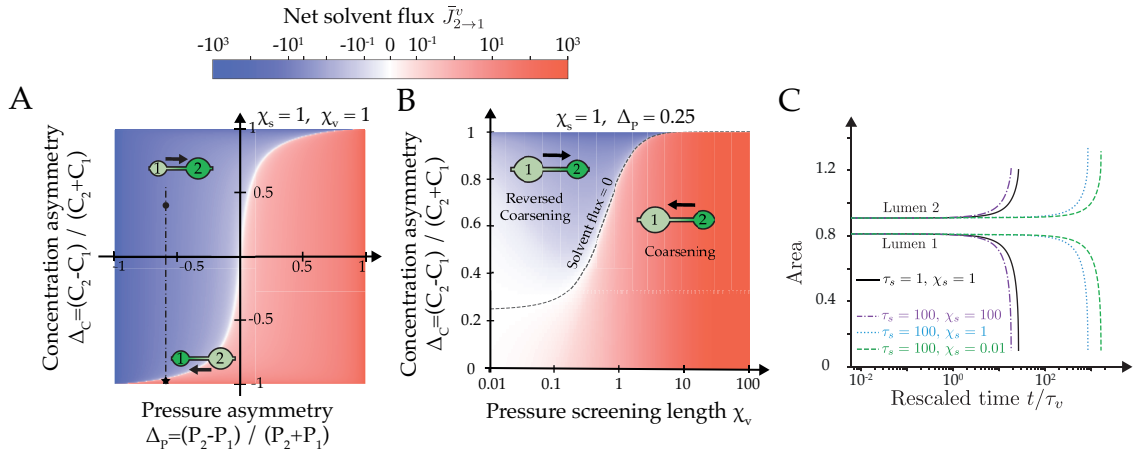

Figure 2. Two-lumen dynamics. (A) Diagram of the net flow $\bar{J}^v_{2\to1} = \bar{J}^v_2 - \bar{J}^v_1$ as a function of concentration and pressure asymmetries Δ_C and Δ_P, for $\chi_{s,v} = 1$. The flow direction is schematized for two sets of values (Δ_P, Δ_C). (B) Diagram of the net flow $\bar{J}^v_{2\to1}$ as function of the concentration asymmetry Δ_C and pressure screening lengths χ_v for $\chi_s = 1$ and $\Delta_P = 0.25$. (C) Time evolution of the area of two lumens as function of χ_s and τ_s. Other simulation parameters are $\chi_v = 10$, $\tau_v = 1\ s$.

where $\delta c(x) = c(x) - c_0$ and $\delta p(x) = p(x) - p_0$ are local concentration and pressure jumps across the membrane. The balance of solutes along the bridge is similarly given by the sum of a longitudinal diffusive flux $e_0 j_d(x) = -e_0 D \frac{\partial \delta c}{\partial x}$ (Fick's law with diffusion coefficient D) and passive lateral fluxes of solutes across the two membrane sides, driven by the imbalance of chemical potential for the solute. Adding an active pumping rate of solutes j^a yields

$$e_0 D \frac{\partial^2 \delta c}{\partial x^2} = 2\mathcal{R}T\lambda_s \log\left(1 + \frac{\delta c}{c_0}\right) - 2j^a \tag{4}$$

where we assumed that the relaxation of concentration in the bridge is very fast compared to other timescales in the problem $\frac{\partial c}{\partial t} \sim 0$ (see Appendix 1). Similarly to ***Dasgupta et al.*** (***2018***), solvent and solute exchanges along the bridge are found to be controlled by two characteristic length scales

$$\xi_v = \sqrt{\frac{\kappa_v}{2\lambda_v}}, \qquad \xi_s = \sqrt{\frac{D e_0 c_0}{2\lambda_s \mathcal{R}T}} \tag{5}$$

which measure the relative magnitude of longitudinal and lateral passive fluxes of solvent (v) and solutes (s) respectively. They play the roles of screening lengths: a pressure (resp. concentration) gradient along the bridge will be screened on a length larger than ξ_v (resp. ξ_s). Therefore, for $\ell \gg \xi_v$ (resp. $\ell \gg \xi_s$), we expect the lumens to become hydraulically (resp. osmotically) uncoupled. On the contrary, for $\ell \ll \xi_{v,s}$, pressure or concentration differences along the bridge may trigger solvent or solute fluxes from one lumen to the other (see Movie 1). In the rest of the manuscript, we will denote by screening lengths the dimensionless ratios $\chi_{s,v} \equiv \xi_{s,v}/\ell_0$, where absolute screening lengths $\xi_{s,v}$ have been rescaled by the mean initial bridge length $\ell_0 = \langle \ell(0) \rangle$. We use these ratios as global parameters to characterize screening effects in our system, but it should be noted that the actual pressure or concentration screening varies in fact in time with the length of the bridge $\ell(t)$. Interestingly, we observed that the ratio $\xi_{v,s}/\ell(t)$ measures roughly the average number of neighbors one lumen can "see" from a hydraulic or osmotic perspective.

To simplify our equations, we remark that the typical hydrostatic pressure jump across the plasma membrane of embryonic cells $\delta P_i \sim \delta p \sim 10^{2-3}$ Pa is a few orders of magnitude lower than the absolute value of osmotic pressure $\Pi_0 = \mathcal{R}Tc_0 \sim 10^5$ Pa. This implies that $\delta C_i, \delta c \ll c_0$ (see Appendix 1) and allows us to derive analytic solutions for solvent and solute fluxes $\pm q(x)$ and $\pm e_0 j_d(x)$ from the bridge equations (3) and (4). By equating these fluxes, evaluated at bridge boundaries $x = \mp\ell(t)/2$ with outgoing fluxes from the lumens J^v_i, J^s_i for $i = 1, 2$, and by fixing the

system size $\mathcal{L}_0 = L_1(t)+L_2(t)+\ell(t) = \text{cte}$, we close our system of equations (see Appendix 1). Denoting L_0 and N_0 the mean initial lumen size and solute number, we introduce the following dimensionless variables $L_i = \bar{L}_i\, L_0$, $\ell = \bar{\ell}\ell_0$, $N_i = \bar{N}_i N_0$, $j^a = \bar{j}^a \lambda_s \mathcal{R}T$, $J_i^v = \bar{J}_i^v \frac{L_0^2}{\tau_v}$, $\bar{J}_i^s = \bar{J}_i^s \frac{N_0}{\tau_s}$, and dimensionless parameters $N_0 = c_0 L_0^2$ and $\epsilon = \frac{\gamma \sin\theta}{L_0 \Pi_0}$. The dynamics of the system reduces finally to four coupled ordinary differential equations (ODEs) for $\bar{N}_i$ and $\bar{L}_i$ $(i = 1, 2)$:

$$\tau_v \frac{d\bar{L}_i}{dt} = \mu v \left[\mu \frac{\bar{N}_i}{\bar{L}_i^2} - 1 - \frac{\epsilon}{\bar{L}_i} \right] - \frac{\mu}{2\bar{L}_i} \bar{J}_i^v \tag{6}$$

$$\tau_s \frac{d\bar{N}_i}{dt} = 2v\bar{L}_i \left[1 - \mu \frac{\bar{N}_i}{\bar{L}_i^2} + \bar{j}^a \right] - \bar{J}_i^s \tag{7}$$

$$1 = \bar{L}_1 + \bar{L}_2 + \bar{\ell} \tag{8}$$

where outgoing fluxes $\bar{J}_i^{v,s} = f_i^{v,s}\left(\bar{N}_{1,2}, \bar{L}_{1,2}, \bar{\ell}\right)$ are functions coupling dynamically the two lumens $i = 1, 2$. The dynamics is controlled by the following solvent and solute equilibration timescales

$$\tau_v = \frac{L_0}{2\lambda_v \Pi_0}, \qquad \tau_s = \frac{L_0 c_0}{2\lambda_s \mathcal{R}T} \tag{9}$$

Hydro-osmotic control of coarsening

To characterize the competition between osmotic and hydraulic effects, we focus first on the factors controlling the instantaneous net solvent flow between two lumens. Any asymmetry in size or tension between two lumens is expected to generate a hydrostatic pressure difference $\delta\bar{P}$, triggering a net solvent flow $\bar{J}_{2\to1}^v = \bar{J}_2^v - \bar{J}_1^v$. But the bridge may also act as an (imperfect) semi-permeable membrane, that can carry osmotically-driven solvent flows if a concentration difference $\delta\bar{C}$ exists between the lumens. These two kinds of solvent flows, hydraulic and osmotic, may enter in competition if $\delta\bar{C}\delta\bar{P} > 0$, as shown in Fig. 2A where we plotted the signed value of the net flow $\bar{J}_{2\to1}^v$ as function of concentration and pressure asymmetries $\Delta_C = (C_2 - C_1)/(C_2 + C_1)$ and $\Delta_P = (P_2 - P_1)/(P_2 + P_1)$. For a given set of screening lengths $\chi_v, \chi_s \sim 1$, the net solvent flow direction expected from Laplace's pressure (from small to large lumens) may be outcompeted by an osmotic flow in the reverse direction if a sufficiently large concentration asymmetry exists between the two lumens. In practice, we observe that the relative asymmetry has to be much larger for concentrations than for pressures to reverse the coarsening direction. This let us anticipate already a limited influence of osmotic gradients, in general, on lumen dynamics. As a further indication for this trend, we find that the magnitude of the solvent flow depends primarily on the pressure screening length χ_v (Fig. 2B), while the screening of concentration asymmetries has no measurable effect for $\chi_s > 1$ and only a mild influence for $\chi_s < 1$ (see Fig. 1). From a dynamical point of view, osmotic effects could however have a strong influence in the limit $\tau_s \gg \tau_v$ and $\chi_s \ll 1$, where solutes are expected to become almost trapped in lumens, their exchange dynamics with the cellular medium and other lumens being largely slowed down. Indeed, if the size of a given lumen drops rapidly, its solute concentration will rise (see Fig. 1B), generating an osmotically-driven solvent flow that may oppose to the pressure-driven flow. This effect, reminiscent of the osmotic stabilization of emulsions and foams by trapped species ***Webster and Cates*** (***1998***, 2001), is illustrated in Fig.2C where we plot the dynamics of two lumens starting at osmotic equilibrium for $\tau_s = 100\tau_v$ and for decreasing values of χ_s from 100 to 10^{-2} ($\chi_v = 10$). In this regime, we observe that the coarsening dynamics is slowed down by a few orders of magnitude through the combined effects of slow solute relaxation and large concentration screening. However, and in contrary to foams or emulsions ***Webster and Cates*** (***1998***, 2001), our system cannot reach complete stabilization, since lumens ultimately homogenize their concentrations by exchanging fluid with surrounding cells.

Influence of active pumping

Then, we explore the influence of active pumping on the dynamics of two lumens. Ion pumps, such as the Na/K ATPase, can actively transport ions from/to the cell against the chemical potential differ-

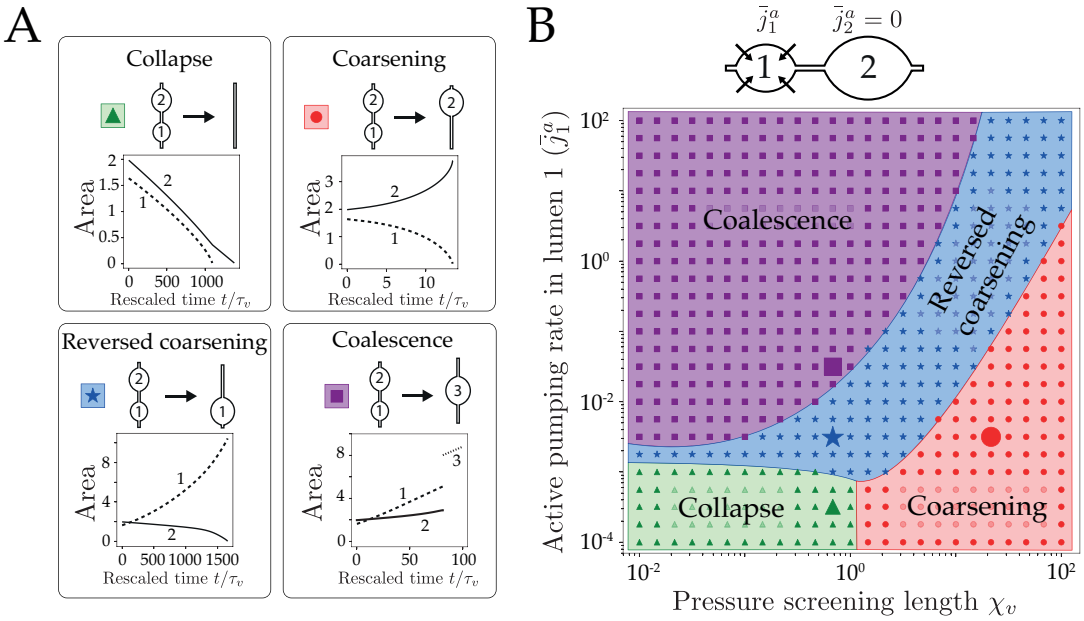

Figure 3. Classification of two lumens dynamics with active pumping. (A) Typical time evolution of the areas of lumen 1 (dotted line) and lumen 2 (full line) in the four cases. (B) Fate diagram for 2 lumens as function of the active pumping $\bar{j}_1^a$ of lumen 1 and pressure screening length χ_v, at fixed $\chi_s = 1$. Four behaviors are found numerically: collapse for large screening and low pumping, coarsening and reversed coarsening at intermediate values and coalescence for large pumping. The delineation of the regions have been drawn by hand, for presentation purpose.

Figure 3–video 1. The four possible dynamics for 2 lumens, corresponding to the four cases highlighted on Fig. 3A; collapse ($\chi_v = 6.8 \times 10^{-1}$, $\bar{j}_1^a = 3.2 \times 10^{-4}$, top left), coarsening ($\chi_v = 2.2 \times 10^{1}$, $\bar{j}_1^a = 3.2 \times 10^{-3}$, top right), reversed coarsening ($\chi_v = 6.8 \times 10^{-1}$, $\bar{j}_1^a = 3.2 \times 10^{-3}$, bottom left) and coalescence ($\chi_v = 6.8 \times 10^{-1}$, $\bar{j}_1^a = 3.2 \times 10^{-2}$, bottom right). Simulation time is shown on top for each simulation. Other model parameters are $\tau_s = \tau_v = 1s$, $\chi_s = 1$ and the lumens are at osmotic equilibrium at time $t = 0$.

ence across the membrane by hydrolyzing ATP. Here, we consider an initial size ratio $L_2(0)/L_1(0) = 1.1$ and a nonzero pumping rate $\bar{j}_1^a$ in the lumen 1 only ($\bar{j}_2^a = 0$). We plot in Fig. 3 the outcome (or fate) of the two lumens as function of $\bar{j}_1^a$ and χ_v. We identify four different possible fates (see Movie 1): collapse of the two lumens (triangles), coarsening $1 \to 2$ (disks), reversed coarsening $2 \to 1$ (stars) and coalescence (squares). At vanishing pumping $\bar{j}_1^a \sim 0$, both lumens are under tension and may either coarsen if their pressure difference is not screened ($\chi_v \gtrsim 1$) or collapse at large pressure screening ($\chi_v \lesssim 1$). When pumping is increased in the lumen 1, a third regime that we called reversed coarsening appears, where the coarsening direction is inverse to the one expected from the initial size asymmetry: this happens when the pumping-driven growth of the lumen 1 overcomes its discharge into the lumen 2, reversing the flow direction. Above some pumping rate a fourth dynamical regime appears, where growth is faster than hydraulic coarsening leading to lumen collision and coalescence. We find therefore that active pumping can greatly modify the dynamics of two lumens, which let us anticipate its major role in the coarsening of a network of lumens.

Coarsening dynamics for a 1-dimensional chain

In this section, we turn to the dynamics of a 1-dimensional chain of $\mathcal{N}$ lumens (Fig. 4A). Each lumen of label i is described by its position, its size $L_i = \sqrt{\mu A_i}$ and its number of moles of solutes N_i, and is connected to up to two neighboring lumens by a bridge (i, j) of length $\ell_{ij}(t)$. The chain has a fixed total length $\mathcal{L}_0 = 2\sum_i L_i(t) + \sum_{\{ij\}} \ell_{ij}(t)$ and its borders are fixed and sealed. We generate initial chain configurations by chosing lumens areas A_i and bridges lengths ℓ_{ij} from Gaussian

distributions of respective means $A_0 = 1$ and $\ell_0 = 10$, and respective standard deviations 0.2 and 2. All our simulations start at osmotic equilibrium ($\delta C_i = \delta c = 0$), and unless otherwise specified we set $\tau_v = \tau_s = 1s$. The coupled ODEs (6) (7) for the lumens $i = 1, ..., \mathcal{N}$ are integrated numerically leading to the typical lumen dynamics shown in Fig. 4A and Movie 1. After a few steps, some lumens may collapse or enter in collision; when such topological events happen, the integration is stopped, the configuration of the chain is recalculated to remove or merge implicated lumens before restarting the integration (see Materials & Methods and Appendix 3).

Coarsening without pumping

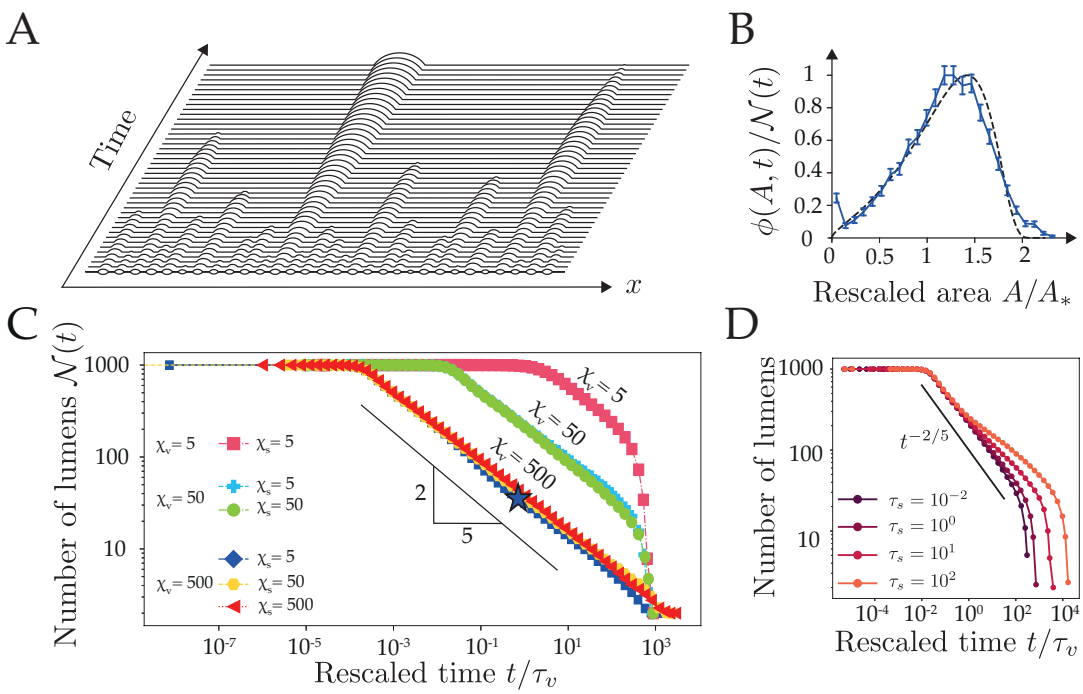

Figure 4. Collective dynamics of a 1-dimensional chain of lumens. (A) Typical spatiotemporal hydro-osmotic coarsening dynamics of a 1-dimensional chain. Here $\mathcal{N}(0) = 30$ lumens evolve from osmotic equilibrium with $\chi_v = 100$, $\chi_s = 1$, $\tau_{s,v} = 1\,s$. (B) Lumen area distribution as function of rescaled area A/A_*, where $A_* = \int A\,\phi(A,t)dA$ is the mean field area with respect to this distribution. The plain curve is an average over 100 simulations with $\chi_v = 500$, $\chi_s = 5$ and taken at the time-point indicated by a star on panel C. The dashed line is the theoretical self-similar distribution given in the SI. (C) Plot of the number of lumens as function of the rescaled time t/τ_v for various values of the screening lengths $\chi_{v,s}$ where each simulation starts at $\mathcal{N}(0) = 1000$ lumens. Each curve is an average of 20 simulations. The scaling law $t^{-2/5}$ (black line) is shown as a guide for the eye. (D) Plot of the number of lumens as function of the rescaled time t/τ_v for $\tau_v = 1\,s$, $\chi_v = 50$, $\chi_s = 5$ and increasing values of the solute relaxation time τ_s from $10^{-2}\,s$ to $10^{2}\,s$. A deviation from the scaling law $t^{-2/5}$ (plotted in plain line as a reference) is observed for large τ_s, indicative of an osmotic stabilization effect, which slows down the coarsening.

Figure 4–video 1. Coarsening dynamics of a chain of 30 lumens without pumping. The simulation time is plotted on top. Due to adaptive time-step, rendering of the simulation "slows down" when a topological events happen. Parameters are $\bar{A}_0 = 1$, $\chi_v = 500$, $\chi_s = 5$, $\tau_s = \tau_v = 1s$. We chose $\bar{\ell}_0 = 1$ for the sake of illustration.

To characterize the average dynamics of a chain, we plot in Fig. 4B the number of lumens as function of time for various values of the initial screening lengths χ_v and χ_s. After a plateau, we generically observe a coarsening behavior characterized by a dynamic scaling law $\mathcal{N}(t) \propto t^{-\frac{2}{5}}$. This scaling exponent is in fact reminiscent of the dynamics of a purely hydraulic chain of droplets ***Pismen and Pomeau*** (***2004***); ***Glasner and Witelski*** (***2005***); ***van Lengerich et al.*** (***2010***). In the limit of small χ_v, we observe yet a rapid collapse of the chain, indicative of the overall uncoupling of lumens. As far as the lumens remain hydraulically coupled to their nearest neighbor, the scaling exponent

remains unaffected by the amplitude of solvent and solute screenings (Fig. 4B). The main difference with a pure hydraulic dynamics can be observed in the onset of coarsening, that is characterized by a typical timescale $T_h = \frac{2\tau_v \ell_0 L_0}{\mu \epsilon \xi_v^2} = \frac{2\ell_0 L_0^3}{\mu \sin\theta \gamma \kappa_v}$ that increases with a decreasing pressure screening length ξ_v. To understand the link between our dynamics and a pure hydraulic system, we consider the limit $\chi_v \gg 1$, $\chi_s \ll 1$, and $\tau_s \ll \tau_v$, where concentrations relax rapidly and lumens are fully coupled hydraulically. In this limit, our system of equations reduces to a single dynamical equation where the contribution of solutes has vanished and that reveals analytically equivalent to the one proposed in ***Glasner and Witelski*** (***2003***); ***Gratton and Witelski*** (***2009***) to describe coarsening in dewetting films (see SI):

$$\frac{dL_i}{dt} = \frac{1}{T_h \ell_{ij} L_i}\left(\frac{1}{L_j} - \frac{1}{L_i}\right) \tag{10}$$

We will refer to this limit as the *hydraulic chain*, where osmotic effects have disappeared. In such limit, the scaling law for the number of lumens $\mathcal{N}(t) \sim t^{-2/5}$ as well as the distribution of lumens size $\phi(A,t)$ can be predicted from a mean-field theory of Lifshitz-Slyosov-Wagner type (see Appendix 2) ***Lifshitz and Slyozov*** (***1961***); ***Glasner and Witelski*** (***2003***); ***Gratton and Witelski*** (***2009***). In Fig. 4C, we compare the size distributions of lumens predicted by the hydraulic chain mean field theory and obtained from our simulations for $\chi_v = 500$, $\chi_s = 5$. The very close agreement indicates that the hydraulic chain limit is generically a good approximation for the behavior of a hydro-osmotic chain. To challenge the validity of the hydraulic chain approximation, we chose parameters favoring the retention of solutes in lumens, as for the two-lumen system (Fig. 2C). In Fig. 4D we plot the time evolution of the chain for increasingly slower solute equilibration (increasing τ_s) and we find indeed a deviation from the scaling law $t^{-2/5}$ when $\tau_s \gg 1\,s$, indicative of a slowing-down of coarsening. Like for the two-lumen system, solutes are transiently trapped within lumens, which triggers larger osmotic asymmetries between lumens that may compete with pressure-difference driven flows and slow down the hydraulic coarsening of the chain (Fig. 1C).

Coarsening with active pumping

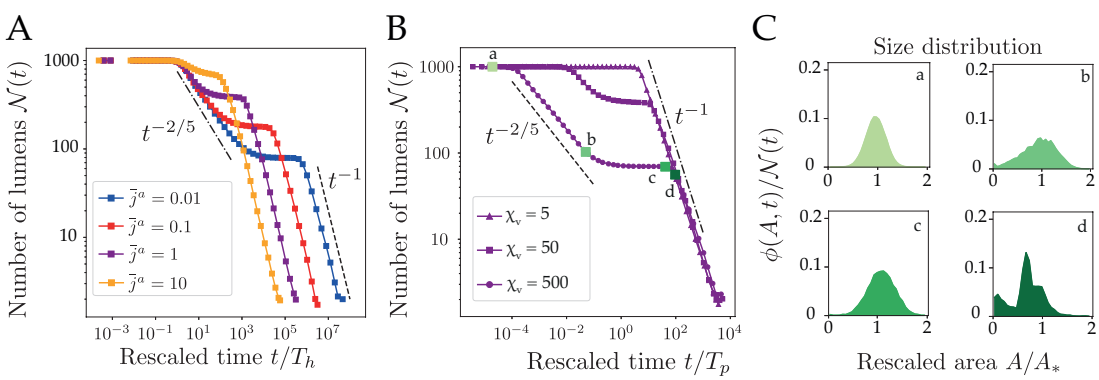

Figure 5. Collective dynamics of a 1-dimensional chain of lumens with active pumping. (A) Coarsening of 1-dimensional chains with uniform active pumping j^a: plot of the number of lumens as function of the rescaled time t/T_h for increasing values of the pumping rate $\bar{j}^a = 10^{-2}, 10^{-1}, 1$ and 10. Each curve is the average over 20 simulations with screening lengths $\chi_v = 50$, $\chi_s = 5$. (B) Number of lumens as function of the rescaled time t/T_p for three values of the pressure screening length χ_v, for $\bar{j}^a = 1$ and $\chi_s = 5$. (C) Area distribution $\phi(A,t)$ at four different times indicated on the plot in (B), with 100 simulations.

Figure 5–video 1. Coarsening dynamics of a chain of 30 lumens with active pumping. The simulation time is plotted on top. Labels indicate the different regimes of the chain hydraulic exchange, plateau, coalescence. Parameters are $\bar{A}_0 = 1$, $\chi_v = 100$, $\chi_s = 1$, $\tau_s = \tau_v = 1s$, $\bar{j}^a = 2$. We chose $\bar{\ell}_0 = 1$ for the sake of illustration.

We finally study the influence of active pumping of solutes on the chain dynamics. We first assume a homogeneous pumping rate $\bar{j}^a$ along the chain. In Fig. 5A we plot the time evolution of the number of lumens $\mathcal{N}$ as function of t/T_h for increasing values of the pumping rate $\bar{j}^a$ from

10^{-2} to 10 ($\chi_{v,s} = 50$). The dynamics is now typically characterized by two coarsening phases that are separated by a novel timescale $T_p = \frac{\tau_v}{\mu \nu j^a} = \frac{\lambda_s L_0 \mathcal{R} T}{2\lambda_v \Pi_0 j^a}$. This timescale measures the competition between active solute pumping, controlled by $\bar{j}^a$, and passive solute relaxation, controlled by λ_s, in triggering solvent permeation, limited by λ_v. For $t \ll T_p$ we recover the hydraulic chain limit characterized by a power-law $t^{-2/5}$ as previously. For $t \gg T_p$, the number of lumens first stabilizes into a plateau before decreasing again with a novel scaling law $\mathcal{N}(t) \sim t^{-1}$. This novel coarsening regime is dominated by lumen coalescence (see Movie 1) and may be understood with the following arguments. Considering the previous hydraulic chain limit ($\chi_v \gg 1$, $\chi_s \ll 1$ and $\tau_s \ll \tau_v$) with nonzero $\bar{j}^a$, we can derive a modified expression for lumen dynamics (see Appendix 2)

$$\frac{dL_i}{dt} = \frac{1}{T_h \bar{\ell}_{ij} L_i} \left[\frac{1}{L_j} - \frac{1}{L_i} \right] + \frac{1}{T_p} \tag{11}$$

In this limit, the last term in (11) is inversely proportional to T_p and corresponds exactly to the rate of osmotic lumen growth triggered by active pumping. Taking the limit $t \gg T_p$, (11) becomes $\frac{dL_i}{dt} \simeq \frac{1}{T_p}$, and using length conservation $\bar{L}_{ij} = \bar{L}_i(t) + \bar{L}_j(t) + \bar{\ell}_{ij}(t)$, it yields $\frac{d\bar{\ell}_{ij}}{dt} \simeq -\frac{2}{T_p}$. The average length of bridges decreases therefore linearly in time, such that the rate of coalescence will naturally scale as $\mathcal{N}(t) \sim (t/T_p)^{-1}$, as shown on Figs. 5A and B. For large enough pumping rate $\bar{j}^a$, we reach a limit where $T_p \sim T_h$, such that the hydraulic coarsening phase disappears, leaving only a coalescence-dominated coarsening dynamics, as we observe on Figs. 5A, B and Movie 1. On Fig. 5C we plot the size distribution of lumens at various time-points of a dynamics where hydraulic and coalescence dominated regimes are well separated in time ($\bar{j}^a = 1$). Starting from the Gaussian used to generate the chain, the distribution first evolves toward the asymmetric distribution characteristic of hydraulic coarsening (Fig. 4C). The transition toward the coalescence phase is characterized by a plateau for the number of lumen and a peaked distribution of lumen sizes, indicative of a collective growth phase with size homogenization of the lumens. This size homogenization can be understood by the fact that lumens become hydraulically uncoupled while coalescence has not yet started, leading to a narrowing of the distribution (see Appendix 2). The coalescence-dominated regime exhibits then a multimodal distribution, that reveals subpopulations of lumens forming by successive waves of coalescence.

Finally, we study how spatial heterogeneities in active pumping within an embryo may bias the position of the final blastocoel. In mammalian embryos, the formation of the blastocoel relies on transepithelial active transport of ions and water from the external medium to the intercellular space by an apico-basally polarized cell layer, the trophectoderm (TE) ***Biggers et al.*** (***1988***); ***Barcroft et al.*** (***2003***). We expect therefore that active pumping may be essentially concentrated at cell interfaces with outer cells (TE), rather than at the ones between inner cells (called ICM for inner cell mass) as illustrated on Fig. 6A. To study the effect of a spatial bias in active pumping, we consider a chain of $\mathcal{N}(0) = 100$ lumens and $\chi_v = 500$, and we perturb an uniform pumping profile with a Gaussian function $\bar{j}^a(x) = \bar{j}_0^a + \frac{\delta \bar{j}^a}{\sqrt{2\pi}\sigma} \exp\left(\frac{(x-\mu)^2}{\sigma^2}\right)$ that is shifted from the chain center ($\mu = 0.4$, $\sigma = 0.05$). We simulate the chain dynamics keeping the amplitude $\delta \bar{j}^a = 1$ of the Gaussian constant and changing the basal uniform value of pumping $\bar{j}_0^a$ only. A uniform pumping profile leads to a typical distribution centered at the middle of the chain. To evaluate the effect of the perturbation with respect to the uniform pumping, we calculate the area below a region of width 4σ centered on the Gaussian and compare it with the area below the remaining quasi-uniform part of the profile of value $\sim \bar{j}_0^a$ (see Fig. 6B). This yields a typical threshold in basal pumping $\bar{j}_0^a = \bar{j}^* \equiv \delta \bar{j}^a \frac{\sigma\sqrt{\pi}}{0.6\text{–}8\sigma} \mathrm{erf}(2)$ (see Appendix 2). For a basal pumping rate $\bar{j}_0^a$ below the threshold $\bar{j}^* \simeq 0.44$, the perturbation dominates and the mean position of the final lumen is shifted to the maximum $x = \mu$ of the Gaussian. On the contrary, when the basal pumping rate $\bar{j}_0^a > \bar{j}^*$, the two effects compete with each others, and the distribution for the final lumen localization may become bimodal (Fig. 6C). In spite of rapid diffusion within the intercellular space, the spatial localization of active pumping can therefore break the radial embryo symmetry by positioning the blastocoel away from the center of the network. In addition to mechanical differences between TE and ICM cells ***Maître et al.*** (***2016***); ***Dumortier et al.***

(*2019*), different rates of pumping between these two types of cells may constitute an alternative and fail-safe mechanism to ensure the robust localization of the blastocoel at the TE interface of mammalian embryos.

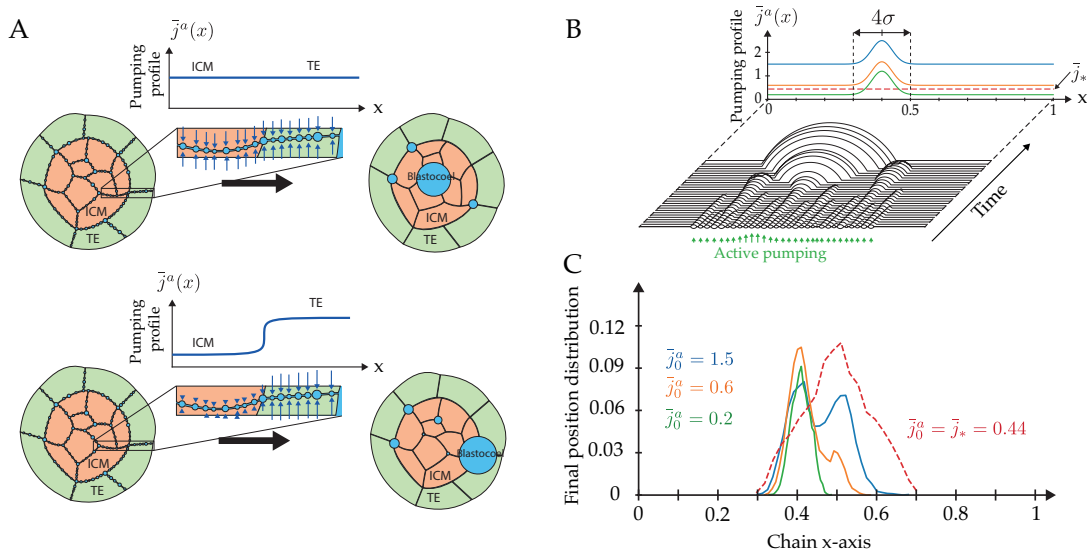

Figure 6. Symmetry breaking from a spatial bias of active pumping. (A) Schematic view of the coarsening outcome with and without spatially heterogeneous active pumping. This heterogeneity in pumping between TE and ICM cell-cell contacts can bias the positioning of the blastocoel toward the TE - ICM interface. (B) Plot of the pumping profiles along the chain and typical chain dynamics ($\mathcal{N}_0 = 30$). The uniform profile corresponds to the threshold $\bar{j}^* \simeq 0.44$ (dashed lines) and perturbed profiles are biased by a Gaussian in the form $\bar{j}^a(x) = \bar{j}_0^a + \frac{\delta \bar{j}^a}{\sqrt{2\pi}\sigma} \exp\left(-\frac{(x-\mu)^2}{\sigma^2}\right)$ with basal pumping rates $\bar{j}_0^a = 0.2,\ 0.6,\ 1.5$ and $\mu = 0.4$, $\sigma = 0.05$, $\delta \bar{j}^a = 1$. (C) Distributions for the localization of the final lumen on a chain of $\mathcal{N}_0 = 100$ lumens, corresponding to the pumping profiles depicted above. Each curve is obtained by averaging 10000 simulations with $\chi_v = 500$, $\chi_s = 1$.

Discussion

We have presented a novel theory for the coarsening of a network of hydro-osmotically coupled biological cavities, that brings several generic, robust and experimentally testable predictions. From a physics perspective, coarsening processes have been the subject of a vast literature, with generally diffusion as the main mode of transport between dynamically coupled compartments ***Lifshitz and Slyozov*** (***1961***). Only a few of them have considered hydrodynamic flows as an alternative mean for mass exchange ***Pismen and Pomeau*** (***2004***); ***van Lengerich et al.*** (***2010***) and the influence of osmotic effects in coarsening have been studied mostly as a mean to stabilize emulsions or foams ***Webster and Cates*** (***1998***, 2001). For a 1-dimensional chain, we find unexpectedly that our hydro-osmotic coarsening model exhibits, for a wide range of solvent and solute permeabilities, the same scaling dynamics $\mathcal{N} \sim t^{-2/5}$ as thin dewetting films, where an ensemble of droplets interacts through a thin fluid layer ***Glasner and Witelski*** (***2003***, 2005); ***Gratton and Witelski*** (***2009***). This indicates that water flows generated by osmotic heterogeneities have generically a mild influence on the coarsening behavior in our model, that is ultimately dominated by hydraulic exchanges, as we hypothesized in ***Dumortier et al.*** (***2019***). Extrapolating this behavior to the realistic topology of microlumens in 3D, that form a continuous 2D network at each cell-cell interface, one would predict a scaling law $\mathcal{N} \sim t^{-3/4}$ for the number of lumens ***van Lengerich et al.*** (***2010***). Whether the slightly more complex topology in embryo and tissues, where cell-cell contacts form themselves a 3D network, might affect the late scaling dynamics remains however to be explored. As this scaling behavior relies essentially on the hydraulic coupling between lumens, one needs to compare the typical diameter of an embryo or small tissue ($50-100\mu$m) with a typical pressure screening length $\xi_v \sim 84\mu$m (see Table

1). In an embryo or small tissue, the microlumens are expected to remain hydraulically coupled during the whole coarsening process, hence ensuring the robust formation of a single cavity. To test and challenge this aspect, it could be interesting to artificially merge two or more embryos before blastulation to see if several, uncoupled, cavities may form. Beyond lumenogenesis, we expect our theory to be relevant for describing the hydraulic cell coarsening phenomena underlying *Drosophila* and *C. elegans* oogenesis ***Alsous et al.*** (***2021***); ***Lamiré et al.*** (***2020***); ***Chartier et al.*** (***2020***). As we showed earlier ***Dumortier et al.*** (***2019***), gradients of cell mechanical properties can be sufficient to spatially bias lumen coarsening, and this mechanism is the main symmetry breaking process put forward to explain cell competition in oogenesis as well. Yet, whether water permeability may affect hydraulic cell couplings through a pressure screening length remains to be tested. It is interesting to note that a similar control of coarsening by stiffness gradients was also recently demonstrated in the context of Ostwald ripening of membrane-less organelles ***Rosowski et al.*** (***2020***); ***Vidal-Henriquez and Zwicker*** (***2020***).

Here, we have shown that active ion pumping may be an additional source of spatial bias for coarsening. Active osmotic volume control emerges hence as a novel mode of symmetry breaking for tissue patterning, that could be relevant also to oogenesis ***Alsous et al.*** (***2021***); ***Lamiré et al.*** (***2020***); ***Chartier et al.*** (***2020***), liquid phase transition of biological condensates ***Jalihal et al.*** (***2021***) and plant tissue growth ***Cheddadi et al.*** (***2019***); ***Long et al.*** (***2020***). Active ion pumping can also largely affect the collective lumen dynamics, with the emergence of a novel coarsening regime dominated by coalescence. If the effect of active pumping may be compared to droplet condensation on a surface ***Viovy et al.*** (***1988***); ***Rogers et al.*** (***1988***), the absence of nucleation in our system constitutes a major difference that precludes a direct comparison of scaling behaviors ***Derrida et al.*** (***1991***); ***Stricker and Vollmer*** (***2015***). The inclusion of lumen nucleation in our model would indeed require a precise microscopic description of the de-adhesion process, coupling membrane mechanics with stochastic binding-unbinding of adhesion molecules ***Kaurin and Arroyo*** (***2019***), that is beyond the scope of this manuscript. The addition of stochastic nucleation and short-time scale cortical and membrane dynamics to our model are undoubtedly interesting avenues to further refine the theory.

One major simplification in our theory is to have neglected the local mechanical response of surrounding cells to lumens deformations. As cell mechanics enters essentially in the small parameter $\epsilon = \frac{\gamma \sin\theta}{L_0 \Pi_0}$ in our model, we do not expect cell mechanics to fundamentally affect the scaling behavior. We have hence verified that the scaling exponent remains unaffected by ϵ, as long as it is smaller than 10^{-1} (see Fig. 2), which is larger than a typical upper estimation $\epsilon < 10^{-2}$ in embryos. A second major assumption of our theory is to have considered only one non-charged solute, while cell volume control is known to rely on a pump-leak mechanism that involves, at minimum, three major ionic species K^+, Na^+ and Cl^- ***Mori*** (***2012***). Our choice was first motivated by the sake of simplicity but turned out to largely ease the numerical treatment of the equations. Indeed, each ion taken individually has a large concentration difference between cytoplasmic and external compartments (K^+ is essentially cytoplasmic while Na^+ and Cl^- are concentrated in the external medium), which would prevent us to asymptotically expand logarithms in the chemical potentials. In contrast, the global osmolarity difference remains generally small compared to its typical absolute value $\delta c \gg c_0$, which allowed us to derive analytic solutions in bridges, and to reformulate the dynamics of the system as coupled ordinary equations to perform extensive numerical simulations. The addition of charged species would require to consider explicitly membrane potentials and electrodiffusion effects, opening novel questions such as the existence of electrical currents and electro-osmotic flows between lumens. These questions are beyond the scope of this manuscript and will require ample effort in terms of theoretical modeling and numerical work. They undoubtedly open exciting novel avenues of research on the still largely overlooked roles of bioelectricity in development and tissue morphogenesis ***Levin*** (***2012***); ***Duclut et al.*** (***2019***).

Methods and Materials

The model equations in the main text are derived in detail in the Appendices, along with additionnal studies.

Coupled differential equations are solved numerically using a Runge-Kutta-Fehlberg method (RKF45) with adaptative time-step ***Fehlberg*** (***1969***); ***Press and Teukolsky*** (***1992***). Topological transitions such as coalescence of two lumens or deletion of an empty lumen are automatically detected and handled by our numerical scheme (see Fig. 1 and Appendix 3 for details). On Fig. 3, the classification of events is determined by the sign of the final slopes for the time evolution of lumen area (see SI for details).

The simulation code and Python notebooks for analysis of the results are available on the following repository: https://github.com/VirtualEmbryo/hydroosmotic_chain

2-lumen Fate classification

Fate corresponds to the first event that occurs for a system of 2-lumens. An isolated lumen with small active pumping $\bar{j}^a < \epsilon/\bar{L}$ will collapse, otherwise it will grow until it occupies the whole chain. Fates are classified depending on the three last steps of the dynamics. The fates are classified as:

- Collapse: both lumens decrease in size. The three last steps of both lumen areas are decreasing.
- Coalescence: a *merge* event is detected, and a new lumen is created, hence stopping the simulation.
- Coarsening: one lumen shrinks, the other grows. If the initially smaller lumen is the one finally growing, the fate is considered as reversed coarsening.

Scaling-law average

Figures 4B, 4D, 5A and 5B show time averages of tens of simulations. Because of different time-stepping from one simulation to another, we defined arbitrarily time points in log-scale at which the number of lumens $\mathcal{N}(t)$ are averaged within these predefined time windows.

Size distributions

Figures 4B, 5C show size-distributions of lumens for $n \geq 100$ simulations. Distributions are calculated at a given simulation time step. Because of different time-stepping from one simulation to another, the closest time is chosen for each realization.

Acknowledgments

We thank Jean-Léon Maître's team for early discussions, Pierre Recho for useful comments on the manuscript, and the Turlier's team members for their support. This work was supported by the Fondation Bettencourt-Schueller, the CNRS-INSERM ATIP-Avenir program, and the Collège de France.

References

Alim K. Fluid flows shaping organism morphology. Philosophical Transactions of the Royal Society B: Biological Sciences. 2018; 373(1747):1–5. doi: 10.1098/rstb.2017.0112.

Alsous JI, Romeo N, Jackson JA, Mason FM, Dunkel J, Martin AC. Dynamics of hydraulic and contractile wave-mediated fluid transport during Drosophila oogenesis. Proceedings of the National Academy of Sciences. 2021; 118(10). doi: 10.1073/pnas.2019749118.

Arroyo M, Trepat X. Hydraulic fracturing in cells and tissues: fracking meets cell biology. Current Opinion in Cell Biology. 2017 feb; 44:1–6. doi: 10.1016/j.ceb.2016.11.001.

Barcroft LC, Offenberg H, Thomsen P, Watson AJ. Aquaporin proteins in murine trophectoderm mediate transepithelial water movements during cavitation. Developmental Biology. 2003; 256(2):342–354. doi: 10.1016/S0012-1606(02)00127-6.

Barua D, Parent SE, Winklbauer R. Mechanics of Fluid-Filled Interstitial Gaps. II. Gap Characteristics in Xenopus Embryonic Ectoderm. Biophysical Journal. 2017; 113(4):923–936. doi: 10.1016/j.bpj.2017.06.063.

Beadle LC. Salt and Water Regulation in the Embryos of Freshwater Pulmonate Molluscs: III. Regulation of Water During the Development of Biomphalaria Sudanica. J Exp Biol. 1969; 20(2):491–499.

Biggers JD, Bell JE, Benos DJ. Mammalian blastocyst: Transport functions in a developing epithelium. American Journal of Physiology - Cell Physiology. 1988; 255(4):419–432. doi: 10.1152/ajpcell.1988.255.4.c419.

Bodenstein L. Simulations of sea urchin early development delineate the role of oriented cell division in the morula-to-blastula transition. Mechanisms of Development. 2020 jun; 162(March):103606. doi: 10.1016/j.mod.2020.103606.

Borland RM, Biggers JD, Lechene CP. Studies on the composition and formation of mouse blastocoele fluid using electron probe microanalysis. Developmental Biology. 1977 jan; 55(1):1–8. doi: 10.1016/0012-1606(77)90315-3.

Cereijido M, Robbins E, Dolan W, Rotunno C, Sabatini D. Polarized monolayers formed by epithelial cells on a permeable and translucent support. Journal of Cell Biology. 1978 jun; 77(3):853–880. doi: 10.1083/jcb.77.3.853.

Chan CJ, Costanzo M, Ruiz-Herrero T, Mönke G, Petrie RJ, Bergert M, Diz-Muñoz A, Mahadevan L, Hiiragi T. Hydraulic control of mammalian embryo size and cell fate. Nature. 2019; 571(7763):112–116. doi: 10.1038/s41586-019-1309-x.

Chartier NT, Mukherjee A, Pfanzelter J, Fürthauer S, Larson BT, Fritsch AW, Kreysing M, Jülicher F, Grill SW. A hydraulic instability drives the cell death decision in the nematode germline. bioRxiv. 2020; doi: 10.1101/2020.05.30.125864.

Cheddadi I, Génard M, Bertin N, Godin C. Coupling water fluxes with cell wall mechanics in a multicellular model of plant development. bioRxiv. 2019; p. 1–16. doi: 10.1101/511717.

Dan K. CYTO-EMBRYOLOGICAL STUDIES OF SEA URCHINS. II. BLASTULA STAGE. The Biological Bulletin. 1952 feb; 102(1):74–89. doi: 10.2307/1538625.

Dan-Sohkawa M, Fujisawa H. Cell dynamics of the blastulation process in the starfish, Asterina pectinifera. Developmental Biology. 1980 jun; 77(2):328–339. doi: 10.1016/0012-1606(80)90478-9.

Dasgupta S, Gupta K, Zhang Y, Viasnoff V, Prost J. Physics of lumen growth. Proceedings of the National Academy of Sciences. 2018 may; 115(21):E4751–E4757. doi: 10.1073/pnas.1722154115.

Derrida B, Godrèche C, Yekutieli I. Scale-invariant regimes in one-dimensional models of growing and coalescing droplets. Physical Review A. 1991 nov; 44(10):6241–6251. doi: 10.1103/PhysRevA.44.6241.

Dolega M, Zurlo G, Goff ML, Greda M, Verdier C, Joanny JF, Cappello G, Recho P. Mechanical behavior of multi-cellular spheroids under osmotic compression. Journal of the Mechanics and Physics of Solids. 2021; 147:104205. https://doi.org/10.1016/j.jmps.2020.104205, doi: 10.1016/j.jmps.2020.104205.

Drasdo D, Forgacs G. Modeling the interplay of generic and genetic mechanisms in cleavage, blastulation, and gastrulation. Developmental Dynamics. 2000 oct; 219(2):182–191. doi: 10.1002/1097-0177(200010)219:2<182::AID-DVDY1040>3.3.CO;2-1.

Duclut C, Sarkar N, Prost J, Jülicher F. Fluid pumping and active flexoelectricity can promote lumen nucleation in cell assemblies. Proceedings of the National Academy of Sciences of the United States of America. 2019; 116(39):19264–19273. doi: 10.1073/pnas.1908481116.

Dumortier JG, Le Verge-Serandour M, Tortorelli AF, Mielke A, de Plater L, Turlier H, Maître JL. Hydraulic fracturing and active coarsening position the lumen of the mouse blastocyst. Science. 2019 aug; 365(6452):465–468. doi: 10.1126/science.aaw7709.

Eckert JJ, Fleming TP. Tight junction biogenesis during early development. Biochimica et Biophysica Acta (BBA) - Biomembranes. 2008 mar; 1778(3):717–728. doi: 10.1016/j.bbamem.2007.09.031.

Edashige K, Tanaka M, Ichimaru N, Ota S, Yazawa Ki, Higashino Y, Sakamoto M, Yamaji Y, Kuwano T, Valdez DM, Kleinhans FW, Kasai M. Channel-Dependent Permeation of Water and Glycerol in Mouse Morulae1. Biology of Reproduction. 2006 apr; 74(4):625–632. doi: 10.1095/biolreprod.105.045823.

Fehlberg E. Low-Order Classical Runge-Kutta Formulas with Stepsize Control and their Application to Some Heat Transfer Problems. NASA Technical Report. 1969; 315.

Fenz SF, Merkel R, Sengupta K. Diffusion and Intermembrane Distance: Case Study of Avidin and E-Cadherin Mediated Adhesion. Langmuir. 2009 jan; 25(2):1074–1085. doi: 10.1021/la803227s.

Fléchon JE, Panigel M, Kraemer DC, Kalter SS, Hafez ESE. Surface ultrastructure of preimplantation baboon embryos. Anatomy and Embryology. 1976; 149(3):289–295. doi: 10.1007/BF00315444.

Friedman AM, Kennedy JW. The Self-diffusion Coefficients of Potassium, Cesium, Iodide and Chloride Ions in Aqueous Solutions. Journal of the American Chemical Society. 1955; 77(17):4499–4501. doi: 10.1021/ja01622a016.

Glasner K, Witelski TP. Coarsening dynamics of dewetting films. Physical Review E - Statistical Physics, Plasmas, Fluids, and Related Interdisciplinary Topics. 2003; 67(1):12. doi: 10.1103/PhysRevE.67.016302.

Glasner KB, Witelski TP. Collision versus collapse of droplets in coarsening of dewetting thin films. Physica D: Nonlinear Phenomena. 2005 sep; 209(1-4):80–104. doi: 10.1016/j.physd.2005.06.010.

Gratton MB, Witelski TP. Transient and self-similar dynamics in thin film coarsening. Physica D: Nonlinear Phenomena. 2009 dec; 238(23-24):2380–2394. doi: 10.1016/j.physd.2009.09.015.

Gustafson T, Wolpert L. Studies on the cellular basis of morphogenesis in the sea urchin embryo. Experimental Cell Research. 1961 jan; 22(C):437–449. doi: 10.1016/0014-4827(61)90120-3.

Hurst PR, Jefferies K, Eckstein P, Wheeler AG. An ultrastructural study of preimplantation uterine embryos of the rhesus monkey. Journal of anatomy. 1978 may; 126(Pt 1):209–20.

Jalihal AP, Schmidt A, Gao G, Little SR, Pitchiaya S, Walter NG. Hyperosmotic phase separation: Condensates beyond inclusions, granules and organelles. Journal of Biological Chemistry. 2021; 296:100044. doi: 10.1074/jbc.REV120.010899.

Kalt MR. The relationship between cleavage and blastocoel formation in Xenopus laevis. II. Electron microscopic observations. Journal of Embryology and Experimental Morphology. 1971; 26(1):51–66.

Kaurin D, Arroyo M. Surface Tension Controls the Hydraulic Fracture of Adhesive Interfaces Bridged by Molecular Bonds. Physical Review Letters. 2019 nov; 123(22):228102. doi: 10.1103/PhysRevLett.123.228102.

Kawagishi R, Tahara M, Sawada K, Morishige K, Sakata M, Tasaka K, Murata Y. Na+/H+ exchanger-3 is involved in mouse blastocyst formation. Journal of Experimental Zoology Part A: Comparative Experimental Biology. 2004; 301(9):767–775. doi: 10.1002/jez.a.90.

Krug SM, Schulzke JD, Fromm M. Tight junction, selective permeability, and related diseases. Seminars in Cell & Developmental Biology. 2014 dec; 36:166–176. doi: 10.1016/j.semcdb.2014.09.002.

Lamiré LA, Milani P, Runel G, Kiss A, Arias L, Vergier B, de Bossoreille S, Das P, Cluet D, Boudaoud A, Grammont M. Gradient in cytoplasmic pressure in germline cells controls overlying epithelial cell morphogenesis. PLOS Biology. 2020 nov; 18(11):e3000940. doi: 10.1371/journal.pbio.3000940.

van Lengerich HB, Vogel MJ, Steen PH. Coarsening of capillary drops coupled by conduit networks. Physical Review E. 2010 dec; 82(6):066312. doi: 10.1103/PhysRevE.82.066312.

Leonavicius K, Royer C, Preece C, Davies B, Biggins JS, Srinivas S. Mechanics of mouse blastocyst hatching revealed by a hydrogel-based microdeformation assay. Proceedings of the National Academy of Sciences of the United States of America. 2018; 115(41):10375–10380. doi: 10.1073/pnas.1719930115.

Lever JE. Inducers of mammalian cell differentiation stimulate dome formation in a differentiated kidney epithelial cell line (MDCK). Proceedings of the National Academy of Sciences of the United States of America. 1979; 76(3):1323–1327. doi: 10.1073/pnas.76.3.1323.

Levin M. Molecular bioelectricity in developmental biology: New tools and recent discoveries. BioEssays. 2012; 34(3):205–217. doi: 10.1002/bies.201100136.

Lifshitz IM, Slyozov VV. The kinetics of precipitation from supersaturated solid solutions. Journal of Physics and Chemistry of Solids. 1961 apr; 19(1-2):35–50. doi: 10.1016/0022-3697(61)90054-3.

Long Y, Cheddadi I, Mosca G, Mirabet V, Dumond M, Kiss A, Traas J, Godin C, Boudaoud A. Cellular Heterogeneity in Pressure and Growth Emerges from Tissue Topology and Geometry. Current Biology. 2020 apr; 30(8):1504–1516.e8. doi: 10.1016/j.cub.2020.02.027.

Løvtrup S. Water permeation in the amphibian embryo. Journal of Experimental Zoology. 1960 nov; 145(2):139–149. doi: 10.1002/jez.1401450203.

Maître JL, Niwayama R, Turlier H, Nédélec F, Hiiragi T. Pulsatile cell-autonomous contractility drives compaction in the mouse embryo. Nature Cell Biology. 2015; 17(7):849–855. doi: 10.1038/ncb3185.

Maître JL, Turlier H, Illukkumbura R, Eismann B, Niwayama R, Nédélec F, Hiiragi T. Asymmetric division of contractile domains couples cell positioning and fate specification. Nature. 2016; 536(7616):344–348. doi: 10.1038/nature18958.

Mazur P, Schneider U. Osmotic responses of preimplantation mouse and bovine embryos and their cryobiological implications. Cell Biophysics. 1986 aug; 8(4):259–285. doi: 10.1007/BF02788516.

Merzdorf CS, Chen YH, Goodenough DA. Formation of Functional Tight Junctions in XenopusEmbryos. Developmental Biology. 1998 mar; 195(2):187–203. doi: 10.1006/dbio.1997.8846.

Miyaguchi K. Ultrastructure of the Zonula Adherens Revealed by Rapid-Freeze Deep-Etching. Journal of Structural Biology. 2000 dec; 132(3):169–178. doi: 10.1006/jsbi.2000.4244.

Mori Y. Mathematical properties of pump-leak models of cell volume control and electrolyte balance. Journal of Mathematical Biology. 2012; 65(5):875–918. doi: 10.1007/s00285-011-0483-8.

Nance J, Priess JR. Cell polarity and gastrulation in C. elegans. Development (Cambridge, England). 2002 jan; 129(2):387–97.

Narayanan V, Schappell LE, Mayer CR, Duke AA, Armiger TJ, Arsenovic PT, Mohan A, Dahl KN, Gleghorn JP, Conway DE. Osmotic Gradients in Epithelial Acini Increase Mechanical Tension across E-cadherin, Drive Morphogenesis, and Maintain Homeostasis. Current Biology. 2020 feb; 30(4):624–633.e4. doi: 10.1016/j.cub.2019.12.025.

Pahlavan AA, Cueto-Felgueroso L, Hosoi AE, McKinley GH, Juanes R. Thin films in partial wetting: Stability, dewetting and coarsening. Journal of Fluid Mechanics. 2018; 845:642–681. doi: 10.1017/jfm.2018.255.

Pismen LM, Pomeau Y. Mobility and interactions of weakly nonwetting droplets. Physics of Fluids. 2004 jul; 16(7):2604–2612. doi: 10.1063/1.1758911.

Powers RD, Tupper JT. Developmental changes in membrane transport and permeability in the early mouse embryo. Developmental Biology. 1977; 56(2):306–315. doi: 10.1016/0012-1606(77)90272-X.

Press WH, Teukolsky SA. Adaptive Stepsize Runge-Kutta Integration. Computers in Physics. 1992; 6(2):188. doi: 10.1063/1.4823060.

Rogers TM, Elder KR, Desai RC. Droplet growth and coarsening during heterogeneous vapor condensation. Physical Review A. 1988 nov; 38(10):5303–5309. doi: 10.1103/PhysRevA.38.5303.

Rosowski KA, Vidal-Henriquez E, Zwicker D, Style RW, Dufresne ER. Elastic stresses reverse Ostwald ripening. Soft Matter. 2020; 16(25):5892–5897. doi: 10.1039/d0sm00628a.

Sigurbjörnsdóttir S, Mathew R, Leptin M. Molecular mechanisms of de novo lumen formation. Nature Reviews Molecular Cell Biology. 2014 oct; 15(10):665–676. doi: 10.1038/nrm3871.

Stricker L, Vollmer J. Impact of microphysics on the growth of one-dimensional breath figures. Physical Review E - Statistical, Nonlinear, and Soft Matter Physics. 2015; 92(4). doi: 10.1103/PhysRevE.92.042406.

Torkko JM, Manninen A, Schuck S, Simons K. Depletion of apical transport proteins perturbs epithelial cyst formation and ciliogenesis. Journal of Cell Science. 2008 apr; 121(8):1193–1203. doi: 10.1242/jcs.015495.

Tuft P. The uptake and distribution of water in the developing amphibian embryo. Symposia of the Society for Experimental Biology. 1965; 19:385–402.

Vidal-Henriquez E, Zwicker D. Theory of droplet ripening in stiffness gradients. Soft Matter. 2020; 16(25):5898–5905. doi: 10.1039/D0SM00182A.

Viovy JL, Beysens D, Knobler CM. Scaling description for the growth of condensation patterns on surfaces. Physical Review A. 1988 jun; 37(12):4965–4970. doi: 10.1103/PhysRevA.37.4965.

Wang AZ, Wang JC, Ojakian GK, Nelson WJ. Determinants of apical membrane formation and distribution in multicellular epithelial MDCK cysts. American Journal of Physiology-Cell Physiology. 1994 aug; 267(2):C473–C481. doi: 10.1152/ajpcell.1994.267.2.C473.

Wang AZ, Ojakian GK, Nelson WJ. Steps in the morphogenesis of a polarized epithelium. I. Uncoupling the roles of cell-cell and cell-substratum contact in establishing plasma membrane polarity in multicellular epithelial (MDCK) cysts. Journal of cell science. 1990 jan; 95 (Pt 1)(1):137–51.

Webster AJ, Cates ME. Stabilization of Emulsions by Trapped Species. Langmuir. 1998; 14(8):2068–2079. doi: 10.1021/la9712597.

Webster AJ, Cates ME. Osmotic Stabilisation of Concentrated Emulsions and Foams. Langmuir. 2001; 17(18):595–608. doi: 10.1021/la000699m.

Wiley LM. Cavitation in the mouse preimplantation embryo: Na K-ATPase and the origin of nascent blastocoele fluid. Developmental Biology. 1984; 105(2):330–342. doi: 10.1016/0012-1606(84)90290-2.

Wolpert L, Tickle C, Arias AM. Principles of development. Oxford University Press, USA; 2015.

Zhang Y, De Mets R, Monzel C, Acharya V, Toh P, Chin JFL, Van Hul N, Ng IC, Yu H, Ng SS, Tamir Rashid S, Viasnoff V. Biomimetic niches reveal the minimal cues to trigger apical lumen formation in single hepatocytes. Nature Materials. 2020; 19(9):1026–1035. doi: 10.1038/s41563-020-0662-3.

Appendix 1

Below we detail the conservation equations in the lumens and bridge following the the notations of Fig. 1D in the main text.

Lumen equations

Force balance

Force balance in a lumen i is given by (i) the tension balance at the junction between the lumen and the bridge, which for an opening angle θ reads

$$\cos\theta = \frac{\gamma_c}{2\gamma}, \tag{12}$$

where γ is the lumen tension, γ_c is the contact (bridge) tension, and (ii) the Laplace's law

$$\delta P_i \equiv P_i - p_0 = \frac{\gamma}{R_i} = \frac{\gamma \sin\theta}{L_i}$$

with $R_i = \frac{L_i}{\sin\theta}$ the radius of curvature of the lumen.

Mass balance

In 2D, the mass corresponds to the area of the lumen $A_i = \frac{L_i^2}{\mu}$, where $\mu = \frac{\sin^2\theta}{2\theta - \sin(2\theta)}$. Mass balance reads

$$\frac{dA_i}{dt} = 4\theta R_i \lambda_v \left[\delta\Pi_i - \delta P_i\right] - J_i^v, \tag{13}$$

where $\delta\Pi_i = \mathcal{R}T(C_i - c_0) \equiv \mathcal{R}T\delta C_i$, is the osmotic pressure jump (or concentration jump $C_i = \frac{N_i}{A_i}$) across the membrane and J_i^v the longitudinal solvent flux toward the bridge. Using the geometrical relationship $L_i = \sqrt{\mu A_i} = R_i \sin\theta$, we can rewrite the equation above as a function of L_i :

$$\frac{dL_i}{dt} = 2\mu\nu\lambda_v \left[\mathcal{R}T\delta C_i - \frac{\gamma\sin\theta}{L_i}\right] - \frac{\mu}{2L_i} J_i^v, \tag{14}$$

where we introduced $\nu = \frac{\theta}{\sin\theta}$. Non-dimensionalization of this equation leads to Eq.[6] in the main text.

Assuming no flux J_i^v, this mass balance equation tells us that at steady-state, the stationary lumen volume is given by $\delta\Pi_i = \delta P_i$, leading to $\frac{\delta C_i}{c_0} = \frac{\gamma}{\Pi_0 R_i} \leq 10^{-2} \ll 1$, where we took $R_i \geq 100\text{nm}$, $\gamma \sim 100\text{pN}/\mu\text{m}$ and $\Pi_0 \sim 10^5\text{Pa}$ (see Table 1). Therefore in the following, we will assume that the concentration jump is small compared to the cellular concentration $\delta C_i \ll c_0$.

Solute balance

Similarly, the change in solute number N_i is due to passive exchanges: across the membrane, driven by chemical potential gradients $\mu = \mathcal{R}T\log(c)$, and toward the bridge via a longitudinal flux J_i^s. An active pumping rate j^a is added at membranes, yielding

$$\frac{dN_i}{dt} = 4\theta R_i \left[\lambda_s \mathcal{R}T \log\frac{c_0}{C_i} + j^a\right] - J_i^s, \tag{15}$$

Using $\delta C_i \ll c_0$, we can expand the log as $\log\frac{1}{1+\delta C_i/c_0} \underset{0}{\sim} -\frac{\delta C_i}{c_0}$ yielding

$$\frac{dN_i}{dt} = 2\nu L_i \left[-\lambda_s \mathcal{R}T\frac{\delta C_i}{c_0} + j^a\right] - J_i^s, \tag{16}$$

Non-dimensionalization of this equation will lead to Eq [7] in the main text.

Bridge equations

The bridge is modeled as a 2-dimensional tube of diameter $e(x,t)$, of length $\ell(t)$. We choose to parametrize the x-axis such that $x \in [-\frac{\ell}{2}, \frac{\ell}{2}]$ for symmetry reasons. Hydrostatic pressure jump between the bridge and the exterior is denoted $\delta p(x,t) = p(x,t) - p_0$, concentration jump $\delta c(x,t) = c(x,t) - c_0$.

Force balance

The membranes have a tension γ_c, and adhesive molecule (cadherins) are distributed along the bridge with line density $\rho(x,t)$, attached to the two membranes, creating an elastic restoring force if the membranes are moved apart. Adding the contribution of the membrane tension, force balance reads :

$$k\rho(x,t)(e(x,t) - e_0) - \gamma_c \nabla^2 e(x,t) = \delta p(x,t), \tag{17}$$

where k is the stiffness of individual cadherins molecules, e_0 is the reference distance between the two membranes, i.e. the bridge diameter.

In the following, we assume that the density and stiffness of cadherin molecules is large enough to ensure a very small deformation of the bridge $e(x,t) \sim e_0$, while keeping the pressure in the bridge $\delta p(x,t)$ of order unity. Therefore, we will neglect spatio-temporal variations in bridge thickness in the next.

Mass balance

The local mass balance in the bridge is given by

$$(e(x+dx,t)dx - e(x,t))dx = [q(x,t) - q(x+dx,t)]\,dt + 2j_v.dx.dt\left[1 + \frac{1}{2}\left(\frac{\partial e(x,t)}{\partial x}\right)^2\right],$$

where j_v is a lateral incoming flux, $q(x,t)$ is the longitudinal hydrodynamic flow along the x-axis, given by 2D Poiseuille flow:

$$q(x,t) = -\kappa_v \frac{\partial \delta p}{\partial x},$$

with κ_v the effective friction, such that $\kappa_v = \frac{e^3(x,t)}{12\eta}$, where η is the solvent viscosity. Lateral flux j_v is given by the imbalances between osmotic and hydraulic pressures with the exterior, such that

$$j_v = \lambda_v(\mathcal{R}T\delta c - \delta p),$$

with λ_v the solvent permeability. Neglecting spatial variations in bridge thickness $e(x,t) \sim e_0$ (thus $\kappa_v = \kappa_v(e_0)$) yields the bridge mass balance Eq.3 in the main text:

$$\kappa_v \frac{\partial^2 \delta p}{\partial x^2} + 2\lambda_v\left[\mathcal{R}T\delta c(x,t) - \delta p(x,t)\right] = 0, \tag{18}$$

Solute balance

The local solute balance in the bridge is given by

$$[\delta c(x,t+dt)e(x,t+dt) - \delta c(x,t)e(x,t)]\,dx = \left[j_d(x,t)e(x,t) - j_d(x+dx,t)e(x+dx,t)\right]dt + 2j_s dt dx\left[1 + \left(\frac{\partial e}{\partial x}\right)^2\right],$$

with the longitudinal diffusive flux given by Fick's law

$$e(x,t)j_d(x,t) = -e(x,t)\,D\frac{\partial \delta c}{\partial x},$$

j_s is the lateral solute incoming flux per unit bridge length, composed of passive (p) and active (a) contributions

$$j_s = j^p + j^a = \mathcal{R}T\lambda_s \log\left(\frac{c_0}{c(x,t)}\right) + j^a,$$

with λ_s the solute permeability coefficient.

In the next, we assume that $\frac{\partial \delta c}{\partial t} \sim 0$, that is that the typical solute diffusion time $\tau_D = \ell_0^2/D$ is very small compared to all other timescales in the system (i.e. $\tau_{v,s}$). Neglecting spatial variations in bridge thickness $e(x,t) \sim e_0$ and assuming small variations in solute concentration $\delta c \ll c_0$, as above, yields the solute balance Eq.4 in the main text:

$$e_0 D \frac{\partial^2 \delta c}{\partial x^2} = 2\lambda_s \mathcal{R}T \frac{\delta c}{c_0} - 2j^a, \tag{19}$$

We give here an estimate for the active pumping flux. From ***Leonavicius et al.*** (***2018***), one has the estimated ion flux generated by the Na/K-ATPase active pumps to be $J_a \simeq 7.8 \times 10^6 ions/min/cell$, at the blastocyst stage, when the cavity is already formed. Assuming their activity is the same at the formation of the micro-lumens, we want to convert J_a into the active pumping constant j^a, expressed as a flux of ions per unit time per unit area ($mol.s^{-1}.m^{-2}$).

At blastocyst stage, the blastocyst volume is estimated to be $0.66 \times 10^6 \mu m^3$ ***Leonavicius et al.*** (***2018***) and has almost spherical shape, giving an estimated surface $3.67 \times 10^4 \mu m^2$, for an average of 42 trophectoderm cells at this stage. This gives a surface of roughly $872 \mu m^2$ per trophectoderm cell. Therefore, one obtains the estimation for the active pumping constant

$$j^a = \frac{7.8 \times 10^6 \text{ions}/(6.022 \times 10^{23} \text{mol}^{-1})}{(60s)(872 \times 10^{-12} m^2)} = 2.47 \times 10^{-10} mol.s^{-1}.m^{-2}$$

Non-dimensionalization

Using the following dimensionless variables: $\delta p = \bar{p}\Pi_0$, $\delta c = \bar{c}c_0$, $x = x'\ell(t)$, $j^a = \bar{j}^a \lambda_s \mathcal{R}T$ yields the two dynamical equations for the bridge

$$\frac{\xi_s^2}{\ell(t)^2}\frac{\partial^2 \bar{c}}{\partial x'^2} = \bar{c}(x') - \bar{j}^a, \tag{20}$$

$$\frac{\xi_v^2}{\ell(t)^2}\frac{\partial^2 \bar{p}}{\partial x'^2} = \bar{p}(x') - \bar{c}(x'), \tag{21}$$

where we have introduced the dimensionless solute (s) and solvent (v) screening lengths $\chi_{s,v}^2(t) = \xi_{s,v}^2/\ell^2(t)$.

Calculation of the boundary fluxes $J^{s,v}$

With (20) and (21), one can find the analytic expressions of the concentration and pressure profiles along the bridge, and therefore explicit formula for solute and solvent fluxes $J_i^{s,v}$ from a lumen.

Concentration profile

The concentration equation (20) in the bridge is similar to a steady-state heat equation with a source term ($\bar{j}^a$) and a radiative term ($\bar{c}(x',t)$). A particular solution is $\bar{c}(x) = \bar{j}^a$ and boundary conditions are given by:

$$\bar{c}(x' = -\frac{1}{2}) = \delta\bar{C}_1 = \mu_1 \frac{\bar{N}_1}{\bar{L}_1^2} - 1, \tag{22}$$

$$\bar{c}(x' = \frac{1}{2}) = \delta\bar{C}_2 = \mu_2 \frac{\bar{N}_2}{\bar{L}_2^2} - 1, \tag{23}$$

which yields the following solution for $\bar{c}(x')$

$$\boxed{\bar{c}(x',t) = \bar{j}^a - (\delta\bar{C}_1 - \bar{j}^a)\frac{\sinh\left[\frac{x'-\frac{1}{2}}{\chi_s(t)}\right]}{\sinh(1/\chi_s(t))} + (\delta\bar{C}_2 - \bar{j}^a)\frac{\sinh\left[\frac{x'+\frac{1}{2}}{\chi_s(t)}\right]}{\sinh(1/\chi_s(t))},} \tag{24}$$

Pressure profile

The pressure equation in the bridge (21) depends on the concentration profile $\bar{c}(x')$ above. Boundary conditions are given by

$$\bar{p}(x' = -\frac{1}{2}) = \delta\bar{P}_1 = \frac{\epsilon_1}{\bar{L}_1}, \tag{25}$$

$$\bar{p}(x' = \frac{1}{2}) = \delta\bar{P}_2 = \frac{\epsilon_2}{\bar{L}_2}, \tag{26}$$

The homogeneous solution is straightforward:

$$\bar{p}_H(x') = \lambda_0 e^{x'/\chi_v} + \mu_0 e^{-x'/\chi_v},$$

To find the particular solution, we use the parameter variation method, introducing the functions $\lambda(x')$ and $\mu(x')$ as

$$\bar{p}(x') = \lambda(x')e^{x'/\chi_v} + \mu(x')e^{-x'/\chi_v},$$

The expression of these functions are

$$\begin{cases} \lambda(x') & = \lambda_a + \int_a^{x'} dy E^-(y), \\ \mu(x') & = \mu_b + \int_b^{x'} dy E^+(y), \\ E^\pm(x') & = \pm\frac{\bar{c}(x')}{2\chi_v}e^{\pm x'/\chi_v}, \end{cases}$$

Using boundary conditions, and choosing $a = \frac{1}{2}, b = -\frac{1}{2}$, we get the final expression of $\bar{p}(x')$

$$\boxed{\begin{aligned} \bar{p}(x) = &-\frac{\delta\bar{P}_1 \sinh\left[\frac{x'-\frac{1}{2}}{\chi_v}\right]}{\sinh(1/\chi_v)} + \frac{\delta\bar{P}_2 \sinh\left[\frac{x'+\frac{1}{2}}{\chi_v}\right]}{\sinh(1/\chi_v)} + \lambda(x')e^{x'/\chi_v} + \mu(x')e^{-x'/\chi_v} + \\ &+ \frac{e^{-1/2\chi_v}}{\sinh 1/\chi_v}\left[\lambda(-\frac{1}{2})\sinh\left(\frac{x'-\frac{1}{2}}{\chi_v}\right) - \mu(\frac{1}{2})\sinh\left(\frac{x'+\frac{1}{2}}{\chi_v}\right)\right], \end{aligned}} \tag{27}$$

The expressions for $\lambda(x')$, $\mu(x')$ can be found analytically

$$\lambda(x') = \int_{\frac{1}{2}}^{x'} E^-(y)dy = \int_{\frac{1}{2}}^{x'}\left(\frac{-\bar{c}(y)}{2\chi_v}e^{-y/\chi_v}\right)dy = \frac{\bar{j}^a}{2}\left[e^{-x'/\chi_v} - e^{-1/2\chi_v}\right] + \frac{\delta\bar{C}_1 - \bar{j}^a}{2\chi_v s_1}I_1^-(x') - \frac{\delta\bar{C}_2 - \bar{j}^a}{2\chi_v s_1}I_2^-(x'),$$

$$\mu(x') = \int_{-\frac{1}{2}}^{x'} E^+(y)dy = \int_{-1/2}^{x'}\left(\frac{\bar{c}(y)}{2\chi_v}e^{y/\chi_v}\right)dy = \frac{\bar{j}^a}{2}\left[e^{x'/\chi_v} - e^{-1/2\chi_v}\right] - \frac{\delta\bar{C}_1 - \bar{j}^a}{2\chi_v s_1}I_1^+(x') + \frac{\delta\bar{C}_2 - \bar{j}^a}{2\chi_v s_1}I_2^+(x'),$$

where, defining

$$s_1 \equiv \sinh\frac{1}{\chi_s}; c_1 \equiv \cosh\frac{1}{\chi_s}; \qquad s^\pm \equiv \sinh\left(\frac{x'\pm\frac{1}{2}}{\chi_s}\right); c^\pm \equiv \cosh\left(\frac{x'\pm\frac{1}{2}}{\chi_s}\right)$$

we find

$$I_1^-(x) = \int_{1/2}^{x} dy e^{-y/\chi_v}\sinh\frac{y-\frac{1}{2}}{\chi_s} = \frac{\chi_v\chi_s}{(\chi_v-\chi_s)(\chi_v+\chi_s)}\left[e^{-x/\chi_v}\left(\chi_v c^-(x) + \chi_s s^-(x)\right) - \chi_v e^{-1/2\chi_v}\right], \tag{28a}$$

$$I_2^-(x) = \int_{1/2}^{x} dy e^{-y/\chi_v} \sinh \frac{y+\frac{1}{2}}{\chi_s} = \frac{\chi_v \chi_s}{(\chi_v - \chi_s)(\chi_v + \chi_s)} \left[e^{-x/\chi_v} \left(\chi_v c^+(x) + \chi_s s^+(x) \right) - e^{-1/2\chi_v} \left(\chi_v c_1 + \chi_s s_1 \right) \right], \tag{28b}$$

$$I_1^+(x) = \int_{-1/2}^{x} dy e^{y/\chi_v} \sinh \frac{y-\frac{1}{2}}{\chi_s} = \frac{\chi_v \chi_s}{(\chi_v - \chi_s)(\chi_v + \chi_s)} \left[e^{x/\chi_v} \left(\chi_v c^-(x) - \chi_s s^-(x) \right) - e^{-1/2\chi_v} \left(\chi_v c_1 + \chi_s s_1 \right) \right], \tag{28c}$$

$$I_2^+(x) = \int_{-1/2}^{x} dy e^{y/\chi_v} \sinh \frac{y+\frac{1}{2}}{\chi_s} = \frac{\chi_v \chi_s}{(\chi_v - \chi_s)(\chi_v + \chi_s)} \left[e^{x/\chi_v} \left(\chi_v c^+(x) - \chi_s s^+(x) \right) - \chi_v e^{-1/2\chi_v} \right], \tag{28d}$$

The denominator is not defined for $\chi_v = \chi_s$, so we calculate the functions $I_{1,2}^{\pm}$ for $\chi_s = \chi_v = X$

$$I_1^-(x) = \frac{1}{2} \left[\left(x - \frac{1}{2} \right) e^{-1/2X} + \frac{X}{2} \left(e^{-2x/X} - e^{-1/X} \right) e^{1/2X} \right], \tag{29a}$$

$$I_2^-(x) = \frac{1}{2} \left[\left(x - \frac{1}{2} \right) e^{1/2X} + \frac{X}{2} \left(e^{-2x/X} - e^{-1/X} \right) e^{-1/2X} \right], \tag{29b}$$

$$I_1^+(x) = \frac{1}{2} \left[\frac{X}{2} \left(e^{2x/X} - e^{-1/X} \right) e^{-1/2X} - \left(x + \frac{1}{2} \right) e^{1/2X} \right], \tag{29c}$$

$$I_2^+(x) = \frac{1}{2} \left[\frac{X}{2} \left(e^{2x/X} - e^{-1/X} \right) e^{1/2X} - \left(x + \frac{1}{2} \right) e^{-1/2X} \right], \tag{29d}$$

Fluxes

Solute fluxes

The dimensionless solute boundary fluxes $\bar{J}_{1,2}^s$ are given by the concentration $\bar{c}(x)$ as

$$\begin{cases} \bar{J}_1^s(t) &= -\frac{\bar{\xi}_s^2}{\bar{\ell}} \partial_{x'} \bar{c}(x')|_{x'=-\frac{1}{2}}, \\ \bar{J}_2^s(t) &= \frac{\bar{\xi}_s^2}{\bar{\ell}} \partial_{x'} \bar{c}(x')|_{x'=\frac{1}{2}}, \end{cases} \tag{30}$$

thus

$$\bar{J}_1^s = \bar{\xi}_s \left[(\delta \bar{C}_1 - \bar{j}^a) \coth \left(\frac{1}{\chi_s} \right) - (\delta \bar{C}_2 - \bar{j}^a) \frac{1}{\sinh \left(1/\chi_s \right)} \right], \tag{31a}$$

$$\bar{J}_2^s = \bar{\xi}_s \left[(\delta \bar{C}_2 - \bar{j}^a) \coth \left(\frac{1}{\chi_s} \right) - (\delta \bar{C}_1 - \bar{j}^a) \frac{1}{\sinh \left(1/\chi_s \right)} \right], \tag{31b}$$

Solvent fluxes

The dimensionless solvent boundary fluxes $\bar{J}_{1,2}^v$ are given by continuity of the pressure

$$\begin{cases} \bar{J}_1^v &= -\frac{\bar{\xi}_v^2}{\bar{\ell}} \partial_{x'} \bar{p}(x')|_{x'=-\frac{1}{2}}, \\ \bar{J}_2^v &= \frac{\bar{\xi}_v^2}{\bar{\ell}} \partial_{x'} \bar{p}(x')|_{x'=\frac{1}{2}} \end{cases} \tag{32}$$

so that

$$\bar{J}_1^v = \bar{\xi}_v \left[\coth \left(\frac{1}{\chi_v} \right) \left(\delta \bar{P}_1 - \lambda (-1/2) e^{-1/2\chi_v} \right) - \frac{1}{\sinh(1/\chi_v)} \left(\delta \bar{P}_2 - \mu (1/2) e^{-1/2\chi_v} \right) - \lambda (-1/2) e^{-1/2\chi_v} \right], \tag{33a}$$

$$\bar{J}_2^v = \bar{\xi}_v \left[\coth \left(\frac{1}{\chi_v} \right) \left(\delta \bar{P}_2 - \mu (1/2) e^{-1/2\chi_v} \right) - \frac{1}{\sinh(1/\chi_v)} \left(\delta \bar{P}_1 - \lambda (-1/2) e^{-1/2\chi_v} \right) - \mu (1/2) e^{-1/2\chi_v} \right], \tag{33b}$$

Limit case

In the limits of vanishing or very large solute/solvent screeninng lengths compared to the bridge length, one obtains :

- For large screening lengths $\xi_{s,v} \gg \ell(t)$, one has

$$\bar{J}_1^s \sim \frac{\bar{\xi}_s^2}{\bar{\ell}} \left[\delta\bar{C}_1 - \delta\bar{C}_2\right] \simeq -\bar{J}_2^s \tag{34}$$

$$\bar{J}_1^v \sim \frac{\bar{\xi}_v^2}{\bar{\ell}} \left[\delta\bar{P}_1 - \delta\bar{P}_2\right] \simeq -\bar{J}_2^v \tag{35}$$

- For small screening lengths $\xi_{s,v} \ll \ell(t)$, one has

$$\bar{J}_i^s \sim \bar{\xi}_s \left(\delta\bar{C}_i - \bar{j}^a\right), \quad i = 1,2 \tag{36}$$

$$\bar{J}_i^v \sim \bar{\xi}_v \delta\bar{P}_i, \qquad i = 1,2 \tag{37}$$

Net fluxes

The net osmotic and solvent fluxes are defined, for the lumens $1,2$, as $\bar{J}_{2\to1}^s = \bar{J}_2^s - \bar{J}_1^s$ and $\bar{J}_{2\to1}^v = \bar{J}_2^v - \bar{J}_1^v$. Using their expressions we find

$$\bar{J}_{2\to1}^s = \bar{\xi}_s \Delta C \coth \frac{1}{2\chi_s}, \tag{38}$$

$$\bar{J}_{2\to1}^v = \bar{\xi}_v \left[\Delta P . \coth \frac{1}{2\chi_v} + \Delta C . \frac{1}{\sinh(\frac{1}{2\chi_v})} . \Lambda(\chi_s, \chi_v)\right], \tag{39}$$

where $\Delta C = \delta\bar{C}_2 - \delta\bar{C}_1$, $\Delta P = \delta\bar{P}_2 - \delta\bar{P}_1$ and

$$\Lambda(\chi_s, \chi_v) = \frac{1}{\sinh\frac{1}{\chi_s}} \frac{\chi_s}{\chi_v^2 - \chi_s^2} \left[\chi_s s_1 \cosh\frac{1}{2\chi_v} - \chi_v(1 + c_1)\sinh\frac{1}{2\chi_v}\right] \tag{40}$$

In the special case where $\chi_s = \chi_v = \chi$, the function Λ reduces to

$$\Lambda(\chi) = \frac{1 - \chi\sinh(\frac{1}{\chi})}{2\chi\sinh(\frac{1}{\chi})} \cosh\left(\frac{1}{2\chi}\right) \tag{41}$$

Moving boundary fluxes

One shall take special care into dealing with the moving boundary problem (Stefan problem). In our case, the border of the lumen moves due to incoming flux, hence the need to state carefully the system. As represented on Fig. 2 we restrict ourselves here to half a lumen, since it is symmetric, and focus on the hydraulic limit. The lumen is centered at X_0, with length L corresponding to the position X_ℓ of its right border. The bridge starts at $X_\ell(t)$ and stops at position X_B. Both X_0, X_B are supposed fixed positions in the reference frame.

First we shall express the half lumen area ($A_{\text{Lumen}}/2$), assuming the lumen is symmetric. This can be expressed as

$$\frac{1}{2}A_{\text{Lumen}}(t) = A_{1/2}(t) + e_0(X_\ell(t) - X_0)$$

but here we do not assume that $e_0 \sim 0$. The bridge has and area $A_B = e_0(X_B - X_\ell(t)$ The lumen generates an outgoing flux $J(t)$, whil the bridge generates an outgoing flux $J_B(t)$.

Assuming no variation in diameter ($e_0 = cte$) of the bridge, the fluxes are equal ($J(t) = J_B(t)$). The total mass/area conservation reads

$$\frac{1}{2}A_{\text{Lumen}} + A_B = -\int dt J_B(t) \tag{42}$$

Thus, derivation of the above equation wrt time leads to

$$\frac{dA_{1/2}}{dt} + e_0\frac{dX_\ell}{dt} - e_0\frac{dX_\ell}{dt} = -J_B$$

and finally

$$\frac{dA_{1/2}}{dt} = -J_B \tag{43}$$

The flux J_B can be expressed as a function of boundary pressures, given it is a Poiseuille flow. Therefore, in spite of the moving character of the boundary, we recover exactly the expression expected for mass conservation in the simplest case of pure hydraulic exchanges without permeability nor osmotic effects. The same reasoning could be applied for this more complex situation as well as for boundary solute fluxes.

Appendix 1 Table 1. Symbols, values and units.

Name	Symbol	Units [2D]	Range [3D]	Units [3D]
Thermal energy per unit mole	RT	$N.m.mol^{-1}$	2.4×10^3	$N.m.mol^{-1}$
Cell concentration[1] (K^+)	c_0	$mol.m^{-2}$	100	$mol.m^{-3}$
Hydrostatic pressure[2]	P	$N.m^{-1}$	$10 - 100$	$N.m^{-2}$
Osmotic pressure	π_0	$N.m^{-1}$	10^5	$N.m^{-2}$
Tension[3]	γ	N	5×10^{-4}	$N.m^{-1}$
Contact angle	θ	-	$\frac{\pi}{3}$	-
Contact tension	γ_c	N	$\sim \gamma$	$N.m^{-1}$
Intercellular space width[4]	e_0	nm	50	nm
Bridge length	ℓ	μm	$0.1 - 10$	μm
Typical lumen length	L_0	μm	$0.1 - 10$	μm
Total length	$\mathcal{L}_0$	μm	$10 - 100$	μm
Water viscosity	η	$N.s.m^{-1}$	10^{-3}	$N.s.m^{-2}$
Water permeability[5]	λ_v	$m^2.s^{-1}.N^{-1}$	7.32×10^{-13}	$m^3.s^{-1}.N^{-1}$
Solute permeability coefficient[6]	λ_s	$mol^2.N^{-1}.s^{-1}.m^{-2}$	10^{-8}	$mol^2.N^{-1}.s^{-1}.m^{-3}$
Solute diffusion constant[7] (KCl)	D	$m^2.s^{-1}$	2.10^{-9}	$m^2.s^{-1}$
Laplace/Osmotic pressures ratio	$\epsilon = \frac{\gamma \sin\theta}{L_0 \Pi_0}$	-	$10^{-2} - 10^{-3}$	–
Effective hydrodynamic friction	$\kappa_v = \frac{e_0^3}{12\eta}$	$m^4.N^{-1}.s^{-1}$	1.04×10^{-20}	$m^5.N^{-1}.s^{-1}$
Pressure screening length	ξ_v	μm	84	μm
Concentration screening length	ξ_s	μm	14	μm
Active pumping flux	j^a	$mol.s^{-1}.m^{-1}$	2.47×10^{-10}	$mol.s^{-1}.m^{-2}$
Solute time	τ_s	s	2	s
Water time	τ_v	s	7	s
Diffusion time	$\tau_D = \frac{\ell_0^2}{D}$	s	10^{-2}	s

References. 1: ***Powers and Tupper*** (***1977***), 2:***Maître et al.*** (***2015***), 3:***Maître et al.*** (***2016***), 4:***Fenz et al.*** (***2009***), 5:***Edashige et al.*** (***2006***), 6:***Dasgupta et al.*** (***2018***) , 7: ***Friedman and Kennedy*** (***1955***)

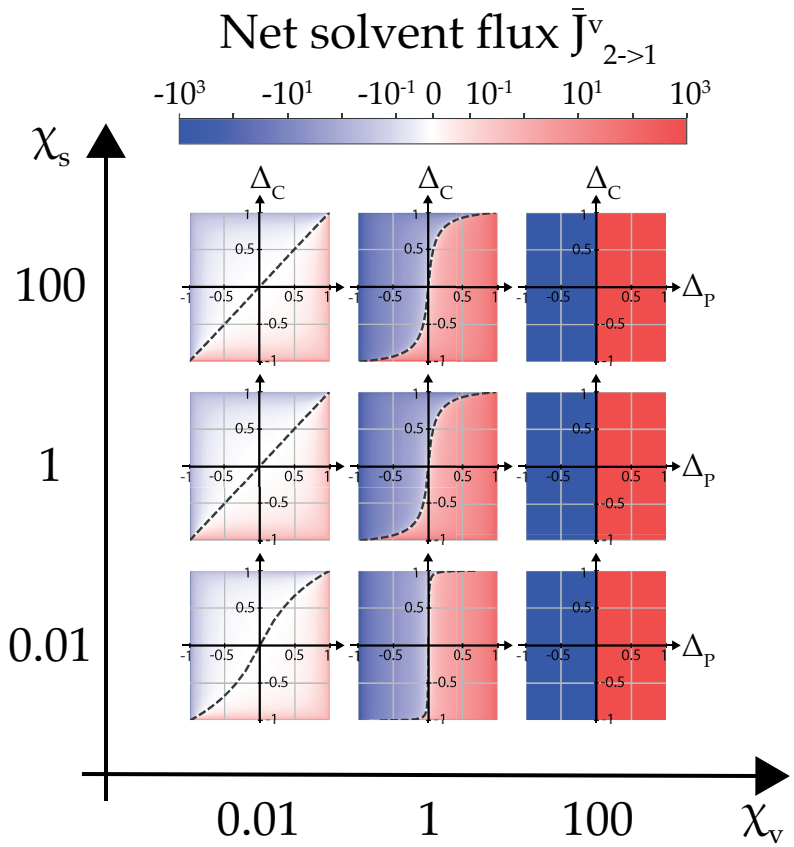

Appendix 1 Figure 1. Net solvent flux diagrams as function of the relative concentration asymmetry Δ_C and pressure asymmetry Δ_P for a 2-lumen system, at different values of the rescaled screening lengths $\chi_{s,v}$. Dashed lines represent the zero net flux $\bar{J}^v_{2\to 1} = 0$. At large pressure screening length $\chi_v = 100$, the net flux does not depends on the concentration screening length χ_s. For smaller pressure screening lengths $\chi_v = 0.01,\ 1$, we observe a mild influence of the concentration screening length when it approaches low values $\chi_s = 0.01$. This shows that the concentration screening length has limited influence on the net solvent fluxes compared to the pressure screening length. Asymmetry ratios are defined in the main text.

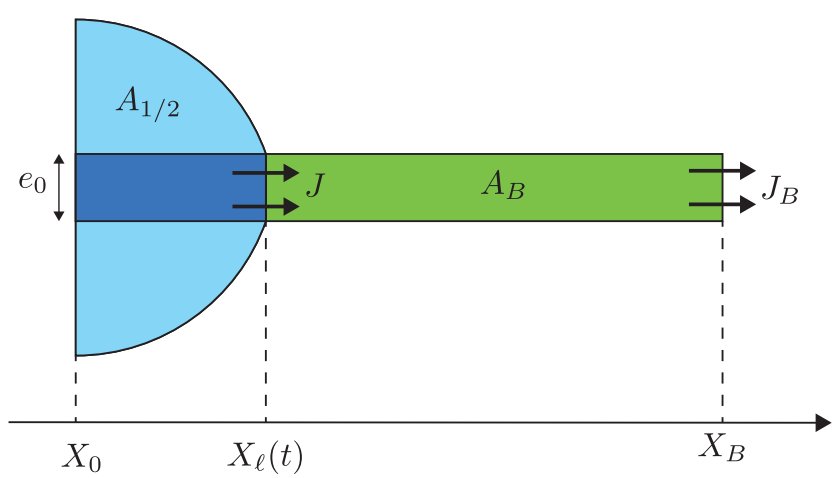

Appendix 1 Figure 2. Half a lumen with moving boundary X_ℓ. The area of half the lumen is $A_{1/2}$ (light blue region) plus the bridge-lumen portion (dark blue region). The green region corresponds to the bridge area.

Appendix 2

We detail here the analytical results for a one-dimensional chain of connected micro-lumens.

Hydraulic limits

We show here how one may reduce the hydro-osmotic model equations for length L_i and number of solutes N_i to a single equation in the appropriate limits.

Without active pumping

We start with two microlumens, labeled i, j, connected by a bridge of dimensionless length $\bar{\ell}_{ij}$. We consider first the case where lumens do not pump solutes ($\bar{j}^a = 0$). Assuming (i) there is no pressure screening $\chi_v \gg 1$, (ii) that solute concentrations are screened $\chi_s \ll 1$ and (iii) that the relaxation time for the number of solutes within lumens is negligible compared to the water relaxation time, $\tau_s \ll \tau_v$, the dimensionless equations Eq. [6-7] reduce to

$$\frac{d\bar{L}_i}{dt} = \frac{\mu\nu}{\tau_v}\left[\delta\bar{C}_i - \frac{\epsilon}{\bar{L}_i}\right] - \frac{\mu}{2\tau_v\bar{L}_i}\frac{\bar{\xi}_v^2}{\bar{\ell}_{ij}}\left[\frac{\epsilon}{\bar{L}_i} - \frac{\epsilon}{\bar{L}_j}\right] \tag{44a}$$

$$\frac{\tau_s}{\tau_v}\frac{d\bar{N}_i}{dt} = -\frac{2\nu\bar{L}_i}{\tau_v}\delta\bar{C}_i \tag{44b}$$

where we used the expressions of fluxes (35) and (36). Because $\tau_s \ll \tau_v$, the left-hand side of the second equation is zero, thus $\delta\bar{C}_i = 0$, the lumens relax immediately to osmotic equilibrium. Since we have $\epsilon \ll 1$, the first term of the right-hand side of the first equation is negligible. Finally, we are left with

$$\frac{d\bar{L}_i}{dt} = -\frac{\mu\epsilon\bar{\xi}_v^2}{2\tau_v\bar{L}_i\bar{\ell}_{ij}}\left[\frac{1}{\bar{L}_i} - \frac{1}{\bar{L}_j}\right] = \frac{1}{T_h\bar{L}_i\bar{\ell}_{ij}}\left[\frac{1}{\bar{L}_j} - \frac{1}{\bar{L}_i}\right] \tag{45}$$

where we define the typical hydraulic time

$$T_h \equiv \frac{2\tau_v}{\mu\epsilon\bar{\xi}_v^2} = \frac{2\tau_v\ell_0 L_0}{\mu\epsilon\xi_v^2} \tag{46}$$

With active pumping

Consider now the case where active pumping is non-zero $\bar{j}^a \neq 0$. Assuming the same limits as before yields now

$$\frac{d\bar{L}_i}{dt} = \frac{\mu\nu}{\tau_v}\delta\bar{C}_i - \frac{\mu}{2\tau_v\bar{L}_i}\frac{\bar{\xi}_v^2}{\bar{\ell}_{ij}}\left[\frac{\epsilon}{\bar{L}_i} - \frac{\epsilon}{\bar{L}_j}\right] \tag{47a}$$

$$0 = \frac{2\nu\bar{L}_i}{\tau_v}\left[\bar{j}^a - \delta\bar{C}_i\right] \tag{47b}$$

Injecting (47b) into (47a) the system of equations reduces to

$$\frac{d\bar{L}_i}{dt} = \frac{\mu\nu}{\tau_v}\bar{j}^a - \frac{\mu\epsilon\bar{\xi}_v^2}{2\tau_v\bar{L}_i\bar{\ell}_{ij}}\left[\frac{1}{\bar{L}_i} - \frac{1}{\bar{L}_j}\right] = \frac{1}{T_h\bar{L}_i\bar{\ell}_{ij}}\left[\frac{1}{\bar{L}_j} - \frac{1}{\bar{L}_i}\right] + \frac{1}{T_p} \tag{48}$$

where we have defined the typical pumping time

$$T_p \equiv \frac{\tau_v}{\mu\nu\bar{j}^a} \tag{49}$$

Mean-field theory of lumen coarsening

Derivation of the scaling law

We present here a mean-field derivation of the scaling law for the number of lumens $\mathcal{N}$ for a linear chain embedded in a space of dimension d. This was first done in ***Gratton and Witelski*** (***2009***) in the case $d = 2$, and we adapt it here to our model, with the lumen size denoted X ($X = A$ in $d = 2$; $X = V$ in $d = 3$). We consider a chain of lumens of total length $\mathcal{L}_0$, assumed to be constant, without active pumping. Let $\phi(X, t)$ be the distribution of drops with size X at time t, such that $\int_X^{X+\Delta X} dX' \phi(X', t)$ is the number of lumens with lsizes between X and $X + \Delta X$. The total number of lumens at time t is

$$\mathcal{N}(t) = \int_0^\infty dX \phi(X, t), \tag{50}$$

The total mass is defined as $M_{\text{tot}} = \sum_i X_i$ in the discrete case, corresponding to the first moment of the distribution. In continuous form, we have

$$M_{\text{tot}} = \int_0^\infty dX X \phi(X, t) \tag{51}$$

The total mass is analoguous to total area in $d = 2$, and to the total volume in $d = 3$. In the case of a purely hydraulic chain, the conservation law is written as

$$\partial_t \phi + \partial_X [\phi u] = 0, \tag{52}$$

with $u = \frac{dX}{dt}$ the rate of change in size of a lumens, given in d dimension by

$$\frac{dX}{dt} = \frac{1}{\bar{\ell}} \left[X_*^{-1/d} - X^{-1/d} \right], \tag{53}$$

where X_* is the mean-field size of the system, defined as $X_*^{-1/d} = \frac{1}{\mathcal{N}} \int_0^\infty dX X^{-1/d} \phi(X, t)$, the harmonic average of the lumen size. The typical distance between two lumens $\bar{\ell}$, or mean separation, can also be expressed as $\bar{\ell} = \mathcal{L}_0 / \mathcal{N}(t)$, and, by definition, the average size of the lumens is defined as $\bar{X} = \frac{1}{\mathcal{N}} \int X \phi(X, t) dX = M_{\text{tot}} / \mathcal{N}(t)$.

Thus, $\bar{\ell} = \bar{X} \mathcal{L}_0 / M_{\text{tot}}$, with the average size $\bar{X}$, which scales like X_*, such that $\gamma = X_* / \bar{X}$. γ, $\mathcal{L}_0$, M_{tot} are supposed to be constant.

We assume that the chain is in the regime in which the distribution ϕ is self-similar, writing it as a scale-invariant self-similar distribution, $\phi(X, t) = t^{-\alpha} f_d(z)$, $z = \frac{X}{X_*}$ and d is the dimension. The mean-field length also has a scaling form $X_* = \sigma t^\beta$, with undetermined constants σ, α, β and γ.

The total mass is written as

$$M_{\text{tot}} = \sigma^2 t^{2\beta - \alpha} \int_0^\infty dz z f_d(z), \tag{54}$$

and the total mass conservation yields $2\beta = \alpha$. Expanding the conservation law terms leads to

$$\beta t^{-2\beta - 1} \left[2 f_d(z) + z f_d'(z) \right] = \frac{M_{\text{tot}} \gamma}{\mathcal{L}_0 \sigma^{2+1/d}} t^{-4\beta - \frac{\beta}{d}} \frac{d}{dz} \left[f_d(z) \left(1 - z^{-\frac{1}{d}} \right) \right] \tag{55}$$

$$\frac{g_1(z)}{g_2(z)} = \frac{C}{\beta} t^{-2\beta - \frac{\beta}{d} + 1}, \tag{56}$$

where $g_1(z) = 2 f_d(z) + z f_d'(z)$, $g_2(z) = \frac{d}{dz} \left(f_d(z)(1 - z^{-1/d}) \right)$, $C = \frac{M_{\text{tot}} \gamma}{\mathcal{L}_0 \sigma^{2+1/d}}$. Since z and t are assumed to be independent variables, then we have $\beta = \left(2 + \frac{1}{d} \right)^{-1}$, and normalizing the

function f, as $\int_0^\infty dz f(z) = 1$, we find the power-law for the number of lumens as

$$\boxed{\mathcal{N}(t) = \sigma t^{-\beta}, \beta = \frac{1}{2 + \frac{1}{d}}} \tag{57}$$

For $d = 2$, we find $\beta = \frac{2}{5}$ ***Gratton and Witelski*** (***2009***), and for $d = 3$, one has $\beta = \frac{3}{7}$, in agreement with ***van Lengerich et al.*** (***2010***) for a linear network of 3D-droplets. Similar arguments can be used to derive the scaling law $\mathcal{N}(t) \propto t^{-3/4}$ for 3D-droplets on a 2D network (instead of a linear chain) ***van Lengerich et al.*** (***2010***).

Mean-field distribution of lumen size

From (57), one may express the function f_d as relation between $f_d(z)$ and its derivative $f_d'(z)$ as :

$$\frac{df_d}{dz} = \left[\frac{\frac{4C}{d\beta} - 8z^{\frac{d+1}{d}}}{4z^{\frac{2d+1}{d}} + \frac{4C}{\beta} z\left(1 - z^{1/d}\right)}\right] f_d(z) \tag{58}$$

In the case $d = 2$, this reduces to the similarity ODE found by ***Gratton and Witelski*** (***2009***), and an explicit solution can be found in ***Pahlavan et al.*** (***2018***). This expression is valid in for $z \in [0, z_{\max}[$, and one may find expressions of C and $z_{\max}$ assuming $z_{\max}$ is an irregular singular point, such that the denominator and its derivative vanish for $z = z_{\max}$. We find the general expressions to be

$$z_{\max} = \left(\frac{d+1}{d}\right)^d; \quad C = \beta d \left(\frac{d+1}{d}\right)^{d+1} \tag{59}$$

which gives for $d = 2$, $\beta = 2/5$, $z_{\max} = \frac{9}{4}$ and $C = \frac{27}{10}$. The function f_2 is plotted on Fig. 4C.

Size distribution of microlumens on the active pumping plateau

We consider a chain with uniform active pumping in the hydraulic limit, and we assume that we are in the regime $t > T_p$. In this regime, we study the part where the number of lumens remains roughly constant, $\mathcal{N}(t) \sim \mathcal{N}_p$, before the coalescence dominated regime. The evolution equation for a single lumen i can be written as $\frac{dL_i}{dt} = \frac{1}{T_p}$. The solution is immediately found to be $L_i(t) = L_i(0) + \frac{t}{T_p}$, where time $t = 0$ is the time at which we consider the start of the regime. The population of lumens corresponds to a distribution with time-dependent mean $\mu(t)$ and standard deviation $\sigma(t)$. By definition, at a given time, one has

$$\mu(t) = \frac{1}{N_p}\sum_{i=1}^{N_p} L_i(t) = \mu(0) + \frac{t}{T_p} \tag{60a}$$

$$\sigma^2(t) = \frac{1}{N_p}\sum_{i=1}^{N_p} (L_i(t) - \mu(t))^2 = \sigma^2(0) \tag{60b}$$

The size distribution of lumens can be approximated by a Gaussian distribution (most likely distribution) with mean $\mu(t)$ and standard deviation $\sigma(t)$:

$$\phi(L, t) \sim \exp\left[-\frac{(L(t) - \mu(t))^2}{\sigma^2(t)}\right] = \exp\left[-\frac{(x(t) - 1)^2}{a^2(t)}\right] \tag{61}$$

where $a^2(t) = \mu^2(t)\sigma^2(t)$ and $x(t) = \frac{L(t)}{\mu(t)}$. Now, in the limit $t \gg 1$, but such that no coalescence nor coarsening event happens,

$$\lim_{t\to\infty} x(t) = 1; \lim_{t\to\infty} a(t) = \infty$$

and the distribution tends to a Dirac distribution :

$$\phi(L,t) \to \delta\left(\frac{L(t)}{\mu(t)} - 1\right)$$

This shows that on the plateau following hydraulic coarsening and coalescence-dominated regime, the distribution evolves to a Dirac distribution centered on the rescaled length $L/\bar{L}$.

Heterogeneous pumping profile

We study the case of a composed pumping profile : a uniform pumping plus a localized gaussian perturbation. Let be $\bar{j}^a(x)$ the pumping profile, defined as

$$\forall x \in [0,1], \bar{j}^a(x) = \bar{j}_0^a + \delta\bar{j}^a e^{-\frac{(x-\mu)^2}{\sigma^2}} \tag{62}$$

where the chain has been rescaled by its total length L_{tot}. The total pumping along the chain, I_{tot}, is given integrating the function along the chain, as

$$I_{\text{tot}} = \int_{x_{\min}}^{x_{\max}} \bar{j}^a(x)dx \tag{63}$$

since in practice, lumens can sometimes not be distributed along the full chain but only within $x_{\min}$ and $x_{\max}$. The effect of localized active pumping is measured comparing the total pumping of two regions : the perturbed (P) versus the constant (C) profile. This is done by the separation of the total pumping into two contributions, provided that we define the perturbed region to lies within $[\mu - n\sigma, \mu + n\sigma]$, where n is an arbitrary integer.

$$I_{\text{tot}} = I_C + I_P = \left[\int_{x_{\min}}^{\mu-n\sigma} \bar{j}_0^a dx + \int_{\mu+n\sigma}^{x_{\min}} \bar{j}_0^a dx\right] + \int_{\mu-n\sigma}^{\mu+n\sigma} \left(\bar{j}_0^a + \delta\bar{j}^a e^{-\frac{(x-\mu)^2}{\sigma^2}}\right) dx \tag{64}$$

with

$$I_C = \int_{x_{\min}}^{\mu-n\sigma} \bar{j}_0^a dx + \int_{\mu+n\sigma}^{x_{\max}} \bar{j}_0^a dx = \bar{j}_0^a\left[\Delta x - 2n\sigma\right] \tag{65}$$

and

$$I_P = \int_{\mu-n\sigma}^{\mu+n\sigma} \left(\bar{j}_0^a + \delta\bar{j}^a e^{-\frac{(x-\mu)^2}{\sigma^2}}\right) dx = 2n\sigma\bar{j}_0^a + \delta\bar{j}^a\sigma\sqrt{\pi}\text{erf}(n) \tag{66}$$

where $\Delta x = x_{\max} - x_{\min}$, and $\text{erf}(x)$ is the error function. Thus, the perturbed region has larger pumping than the constant region if

$$\begin{aligned} I_P > I_C &\Leftrightarrow 2n\sigma\bar{j}_0^a + \delta\bar{j}^a\sigma\sqrt{\pi}\text{erf}(n) > \bar{j}_0^a\left[\Delta x - 2n\sigma\right] \\ &\Leftrightarrow \delta\bar{j}^a\sigma\sqrt{\pi}\text{erf}(n) > \bar{j}_0^a\left[\Delta x - 4n\sigma\right] \\ &\Leftrightarrow \frac{\delta\bar{j}^a\sigma\sqrt{\pi}\text{erf}(n)}{\Delta x - 4n\sigma} > \bar{j}_0^a \end{aligned}$$

which gives us the threshold $\bar{j}*$ as

$$\bar{j}_* = \frac{\delta\bar{j}^a\sigma\sqrt{\pi}}{(x_{\max} - x_{\min}) - 4n\sigma}\text{erf(n)} \tag{67}$$

In Fig. 6, we have $n = 2$, $x_{\min} = 0.2$, $x_{\max} = 0.8$, $\sigma = 0.05$, $\delta\bar{j}^a = 1$, that gives $\bar{j}^* \simeq 0.44$.

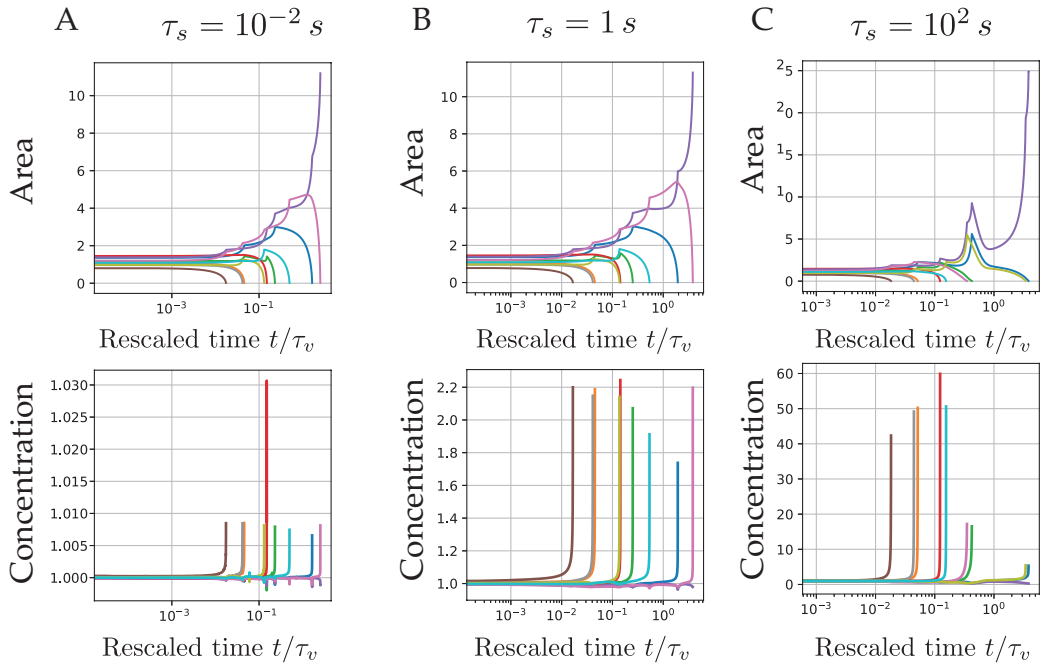

Appendix 2 Figure 1. Typical dynamics of a chain with $\mathcal{N}(0) = 10$ lumens. (A) With parameters $A_0 = 1$, $\ell_0 = 10$, $\chi_v = 50$, $\chi_s = 5$, $\tau_v = 1\ s$, $\tau_s = 0.01\ s$. (B) With parameters $\chi_v = 50$, $\chi_s = 5$, $\tau_v = 1\ s$, $\tau_s = 1\ s$. (C) With parameters $\chi_v = 50$, $\chi_s = 5$, $\tau_v = 1\ s$, $\tau_s = 100\ s$.

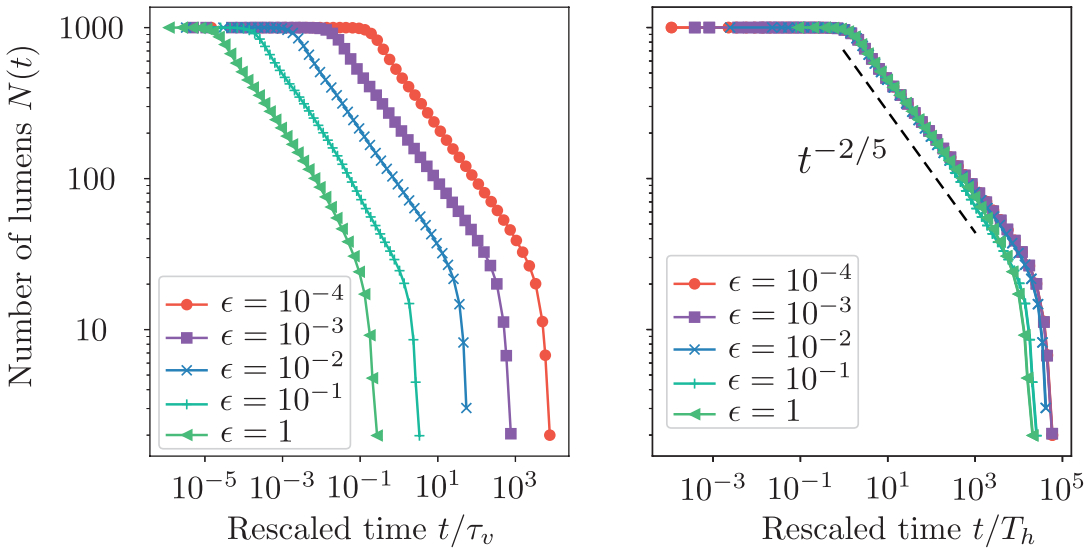

Appendix 2 Figure 2. Influence of cell mechanics on coarsening: the parameter ϵ is varied from 10^{-4} to 1. (Left) Number of lumens as function of the rescaled time t/τ_v, showing the influence of ϵ on the hydraulic time T_h. (Right) Number of lumens as function of the rescaled time t/T_h. All the curve collapse but a small deviation from the scaling law $t^{-2/5}$ is observed for $\epsilon \gtrsim 10^{-1}$. The scaling law $\mathcal{N}(t) \sim t^{-2/5}$ is shown as a dashline. Parameters are $\chi_v = 50, \chi_s = 5, \tau_s = \tau_v = 1s$ and $\mathcal{N}(0) = 1000$. Each curve is an average of 20 simulations.

Appendix 3

Chain integration

Chain generation

Chains are generated with normal distributions for the areas of lumens, $A_i \hookrightarrow \mathcal{N}(A_0, \sigma_A)$ and bridges $\ell_{i,j} \hookrightarrow \mathcal{N}(\ell_0, \sigma_b)$, with usually $A_0 = 1$ ($L_0 = \sqrt{\mu A_0} \simeq 0.78$), $\ell_0 = 10$ (indicated otherwise). The total length of the chain is given by $\mathcal{L}_0 = 2\sum_i L_i + \sum_{i,j} \ell_{i,j}$ and its conservation is used as a check for topology. The number of ions in a lumen is denoted N_i, and is choosen at osmotic equilibrium such that $N_i = \frac{\mathcal{L}_i^2}{\mu_i}$ or randomly with normal distribution $\mathcal{N}(N_0, \sigma_N)$.

The rescaled screening lengths $\chi_{s,v}$ are considered as input parameters, and the non-dimensionalized screening lengths $\xi_{s,v}$ are calculated according to the average bridge length ℓ_0.

Numerical scheme

The algorithm is composed of two important parts : the integration of ordinary differential equations (ODE) that solves the dynamic of the chain, and the topology, that handles events when a cavity disappear or fuse with another. It is schematically represented in Fig. 1.

Initialization

First, the chain is initialized with the imported parameters from a config file. This is done using a homemade parser. Once the parameters imported, the chain is generated either randomly (with a seed if specified) or according to the given files (see examples in _configfiles folder). The status of the chain, either hydraulic (H) or hydroosmotic (HO), must be specified. Pumping profile (if specified) is also computed at that time.

Integration

After generation, the ODEs are solved iteratively, with a given solver, either Runge-Kutta 45 (RK45) or Runge-Kutta-Felhberg 45 (RKF45, default).

The RKF45 method Numerical integration for a system of ODE with initial value problem (IVP) often uses Runge-Kutta (RK) methods, based of iterative integration. The classical method is known as RK45. In order to improve integration, Fehlberg ***Fehlberg*** (***1969***) proposed a new way to obtain a fourth-order method, with error of order 5, hence known as Runge-Kutta-Felhberg or RKF45. If we consider the IVP

$$\frac{dy}{dt} = f(t, y(t)), \quad y(t=0) = y_0$$

with $y(t)$ a time-dependent variable and f is a given function. The time interval may be discretized with a time-step Δt, such that $t_{i+1} = t_i + \Delta t$, and similarly $y_i = y(t_i)$. RKF45 proposes a first estimation for the next value y_{i+1} given the time step and previous step y_i, as

$$y_{i+1} = y_i + \frac{25}{216}k_1 + \frac{1408}{2565}k_3 + \frac{2197}{4104}k_4 - \frac{1}{5}k_5,$$

with the weights

$$\begin{cases} k_1 &= \Delta t f(t, y_i) \\ k_2 &= \Delta t f(t_i + \frac{1}{4}\Delta t, y_i + \frac{1}{4}k_1) \\ k_3 &= \Delta t f(t_i + \frac{3}{8}\Delta t, y_i + \frac{3}{32}k_1 + \frac{9}{32}k_2) \\ k_4 &= \Delta t f(t_i + \frac{12}{13}\Delta t, y_i + \frac{1932}{2197}k_1 - \frac{7200}{2197}k_2 + \frac{7296}{2196}k_3) \\ k_5 &= \Delta t f(t_i + \Delta t, y_i + \frac{439}{216}k_1 - 8k_2\frac{3680}{513}k_3 - \frac{845}{4104}k_4) \\ k_6 &= \Delta t f(t_i + \frac{1}{2}\Delta t, y_i - \frac{8}{27}k_1 + 2k_2 - \frac{3544}{2565}k_3 + \frac{1859}{4104}k_4 - \frac{11}{40}k_5) \end{cases}$$

Error evaluation and Adaptive time-stepping RKF45 method also finds another estimate of the next step y_{i+1}, that we will denote z_{i+1}, and is given by

$$z_{i+1} = y_i + \frac{16}{135}k_1 + \frac{6656}{12825}k_3 + \frac{28561}{56430}k_4 - \frac{9}{50}k_5 + \frac{2}{55}k_6,$$

Therefore, we can define an error ϵ as

$$\epsilon = |y_i - z_i|,$$

For large variations of the variable $y(t)$, the two estimates give a large error, and conversly, a small error for small variations. This error allows us to calculate a new time step Δt_{i+1} such that ***Press and Teukolsky*** (***1992***)

$$\Delta t_{i+1} = \begin{cases} \Delta t_i S \left(\frac{\tau}{\epsilon}\right)^{0.2}, & \text{if } \epsilon > \tau \\ \Delta t_i S \left(\frac{\tau}{\epsilon}\right)^{0.25}, & \text{if } \epsilon \leq \tau \end{cases} \tag{68}$$

where Δt_i is the previous time-step, S is a security factor (arbitrary factor, usually $S = 0.9$), τ is the tolerance (arbitrary factor, usually $\tau \sim 10^{-6}$ in the litterature, we use $\tau \sim 10^{-10}$ to prevent divergences). Thus, if the error is higher than the tolerance, the time-step is reduced, otherwise it increases.

For both $RK45$ and $RKF45$ cases, we have one set of weights ($\{k^{(j)}\}$ for L_j's) for H-chain, or two sets ($\{k^{(j)}, q^{(j)}\}$ for L_j's and N_j's) for HO-chain. Note that because the lumens are not moving during integration, the constraint $L_a + L_b + \ell_{ab} =$ cste must be enforced in the calculation of the weights. Since topological events modify the ODE equations, one cannot let them happen during integration. At the end of the weights calculation, a check is performed on the lengths of bridges and lumens. While topological event happens (merge or collapse), the integration is restarted from the previous time-step with a new halved time-step. This is a costly procedure, but required in order to avoid wrong results. The new time step is calculated at the end of the integration. For RK45, it is given by $\Delta t_{i+1} = \alpha / N(t_i^{\beta})$. For RKF45, it is given according to (68). The error ϵ is calculated over the estimations of the lengths L_j, since divergences occur for at small lengths due to concentration and pressure terms. For estimations $y_{i+1}(L_j)$ and $z_{i+1}(L_j)$ of the length L_j at step $i+1$, the error ϵ is the maximum of the ϵ_j's :

$$\epsilon = \max_j \epsilon_j = \max_j |y_{i+1}(L_j) - z_{i+1}(L_j)|, \tag{69}$$

τ can be changed in the config file. The security factor $S = 0.90$ is a constant.

Topology

When an integration step is complete and valid, topology is checked. We assume all topological events to be instantaneous.

1. We first check whether lumens disappear. A lumen i collapses if its length is below a given threshold L_{dis}
$$L_i \leq L_{\text{dis}}, \tag{70}$$
The value of L_{dis} is defined in the config file. We choose $L_{\text{dis}} = 0.1$ in order to avoid divergence of the concentration when a lumen shrinks. When a lumen collapses, it is removed from the graph, as well as the bridges that connected it. Its two neighbors are connected via a new bridge, but they do not move.
2. We then check whether a lumen collides with the chain borders. If a lumen i overlaps the border, it will be pushed towards the center, say ℓ_{0i} at left border. This is done by checking the length of the bridge between the lumen i and the border, considered as a lumen. Assuming the lumen i touches the left border (index 0), the new position x_i' of the center of mass of the lumen is moved towards the center if
$$\ell_{0i} < 0 \Rightarrow x_i' = x_i + \ell_{0i}, \tag{71}$$
This works the same for the right border (index -1), such that $\ell_{i,-1} < 0 \Rightarrow x_i' = x_i - \ell_{i,-1}$.
3. Finally, we detect collisions between lumens. Two colliding lumens merge together, forming a new lumen. A collision between parent lumens i, j is detected when
$$\ell_{ij} \leq \ell_{\text{merge}}, \tag{72}$$
where ℓ_{merge} is a length that is defined in the config file. We usually choose $\ell_{\text{merge}} = 10^{-3}$. When a collision occurs, a new lumen is created with index k, while parent lumens i, j are deleted from the graph. The center of mass of the new lumen k is given by the barycenter of the two parent lumens:
$$x_k = \frac{x_i A_i + x_j A_j}{A_i + A_j}, \tag{73}$$
where x is the position and A the area (equivalent to mass) of a lumen. The area of new lumen k is calculated to conserve mass:
$$A_k = A_i + A_j, \tag{74}$$
and its length is calculated accordingly. If the lumen is hydro-osmotic, its total number of ions is conserved:
$$N_k = N_i + N_j, \tag{75}$$
Finally, if a profile $f_p(x)$ of active pumping is imposed, the new active pumping j_k^a is given by the position x_k, such that
$$j_k^a = \frac{1}{|x_2 - x_1|} \int_{x_1}^{x_2} f_p(x) dx,$$
where x_1, x_2 are the positions of the borders of the lumen or the bridge. Otherwise, it is the average of the active pumping constants of merging lumens, $j_k^a = \frac{1}{2}(j_i^a + j_j^a)$. New bridges between neighbors of lumens i and j are created and their lengths are given by L_k and x_k.
4. Since multiple lumens could merge at the same time, a loop detects whether there are still collisions occurring after the merging of lumens and redefinition of the connectivity graph.

At the end of the topology check, the algorithm checks whether stop conditions are fulfilled. Usually, the integration is stopped when $\mathcal{N}(t) \leq 1$, or if one lumen occupies the whole chain.

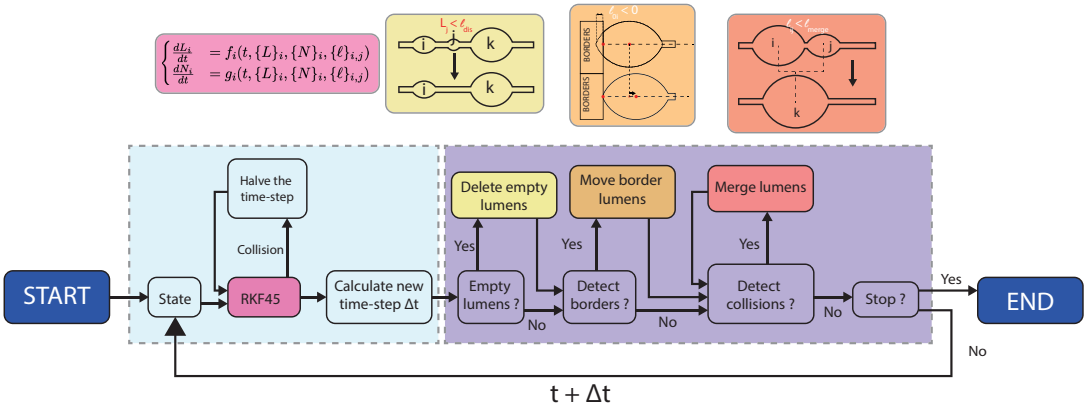

Appendix 3 Figure 1. Representation of the numerical scheme.